Optics and Optoelectronics of Atomically Thin Magnets and Semiconductors

Genevieve Clark

A dissertation

submitted in partial fulfillment of the

requirements for the degree of

Doctor of Philosophy

University of Washington

2018

Reading Committee:

Xiaodong Xu, Chair

Daniel Gamelin

Peter Pauzauskie

Program Authorized to Offer Degree:

Materials Science & Engineering

University of Washington

Abstract

Optics and Optoelectronics of Atomically Thin Magnets and Semiconductors

Genevieve Clark

Chair of the Supervisory Committee:
Associate Professor Xiaodong Xu
Physics and Materials Science & Engineering

Since the discovery of graphene, layered van der Waals materials have become one of the most active subjects of study. The array of available atomically thin materials has expanded rapidly beyond graphene, encompassing a wide variety of physical properties ranging from insulators like hexagonal boron-nitride, to semiconductors such as MoS_2 and superconductors (ie $NbSe_2$) to name a few. These materials are of significant fundamental interest, since they offer the first opportunity to study physical phenomena in a truly two-dimensional system, while showing layer-dependent emergent properties unavailable in any other class of materials. They also offer a potential answer to the increasing demand for nanostructured materials, as current electronic and magnetic devices approach the nanoscale, and devices based on quantum mechanical phenomena rise to the forefront of emerging technology. Here, I employ optical and optoelectronic characterization to study two

different types of 2D materials - few-layer flakes of the layered magnetic insulator CrI_3, and monolayer flakes of semiconducting WSe_2.

The first three chapters of this thesis focus on the isolation, characterization, and control of magnetism in mono- and few-layer flakes of CrI_3. Bulk crystals of CrI_3 are known to be ferromagnetic insulators with large predicted magnetocrystalline anisotropy, essential in order to stabilize low dimensional magnetic order against thermal fluctuations. Optical characterization of monolayer CrI_3 reveals robust ferromagnetic behavior, while bilayer and trilayer flakes show layered antiferromagnetic behavior, with strong intra-layer ferromagnetism and antiferromagnetic inter-layer coupling. Van der Waals heterostructure devices based on bilayer CrI_3 flakes allow gate-dependent control of magnetic behavior in bilayer CrI_3 flakes. This work demonstrates both the first truly two-dimensional magnetic material and electrostatic control of magnetic phase in bilayer CrI_3.

In chapter four, I discuss the optical properties of both intrinsic and defect-bound excitons in monolayers of WSe_2 scalably grown using chemical vapor deposition (CVD). While the majority of optical studies utilize exfoliated flakes of WSe_2, this time-consuming and non-scalable process will limit future studies of this material. I discuss a scalable, direct method of monolayer growth that yields flakes with high optical quality, assessed using low-temperature optical characterization of the intrinsic excitons in this material. I then discuss the discovery of a new type of single photon emitter found in the monolayer flakes, thought to arise from single intrinsic excitons localized to defects within the layers. Finally, these two materials are combined to form spintronic devices based on van der Waals heterostructures of bilayer CrI_3 and monolayer WSe_2 described in chapter 5.

TABLE OF CONTENTS

LIST OF FIGURES

ACKNOWLEDGEMENTS

I would like to thank my principal investigator and research advisor Xiaodong Xu for his outstanding guidance and support during my PhD. His mentorship and intellectual contributions are unmatched. I would also like to thank Professors David Cobden and Kai-Mei Fu for enlightening discussions and advice, as well as the use of their lab equipment. I would also like to thank Professors Di Xiao and Wang Yao for their theoretical guidance, and Dr. Michael McGuire and Professor David Mandrus for crystal growth.

I would like to thank Professor John Schaibley for his guidance and assistance with optical measurements and experimental insight throughout my years as a graduate student.

Finally I would like to thank Dr Grant Aivazian, Dr Mitchell Jones, Dr. Harold Cai, Dr. Colin Chow, Dr Jason Ross, Dr Sanfeng Wu, Kyle Seyler, Pasqual Rivera, Nathan Wilson, and Bevin Huang for their advice and assistance with optical measurements and fabrication.

Chapter 1. MAGNETISM IN 2D SYSTEMS

Magnetic phenomena and materials have been the focus of fundamental studies for over a century, spurring enormous technological advancement including the development of magnetic recording and data storage media[1]. As a result, there has been significant effort to realize magnetic behavior in one- and two- dimensional systems, an increasingly crucial goal as device components rapidly approach the nanoscale. In this chapter I describe previous theoretical and experimental studies of magnetic behavior in low dimensional systems, and how this work informs the investigation of low dimensional magnetism in 2D materials.

1.1 THEORETICAL STUDIES

Theoretical interest in low-dimensional magnetic behavior began early in the 1900's, amid a push to understand the existence or absence of phase transitions in low dimensional systems, using simplified statistical mechanical models[2,3]. Phase transitions driven by an external variable (for example temperature), are typically characterized by a change from a disordered high temperature phase to a low temperature ordered phase occurring at some critical temperature T_c[4]. This transition to an ordered phase involves a spontaneous symmetry breaking from the isotropic disordered phase to an anisotropic ordered phase characterized by lower symmetry, occurring at the critical temperature. This symmetry breaking and onset of the ordered phase is characterized by an order parameter, which is zero above the critical temperature and non-zero below Tc. In the case of a ferromagnetic material, the order parameter is the magnetization $M(T)$. Above the Curie temperature, the magnetization is zero and the system is isotropic. As it is cooled through Tc, $M(T)$ becomes non-zero, introducing a polarization along the axis of spontaneous magnetization. This anisotropy lowers the overall symmetry of the system to that of the low temperature, ordered

state. For any order-disorder phase transition, the behavior of the order parameter as a function of temperature near Tc can be expressed as a power law characterized by a critical exponent β. In the case of magnetic materials, this has the form[5]:

$$M_0(T) = (T - T_c)^{\beta}$$

Where T_c is the Curie temperature and M_0 is the spontaneous magnetization. Based on the theory of phase transitions and the universality hypothesis, the thermodynamic behavior of systems near a phase transition depends on a small number of factors including dimensionality and symmetry, but not the microscopic nature of the system. Systems can be grouped into universality classes displaying the same thermodynamic behavior, and characterized by the same set of critical exponents (including β)[5,6]. These critical exponents characterize the behavior of physical parameters of the system (i.e. the order parameter) in the neighborhood of the phase transition, and also provide insight into the dimensionality of the system and its symmetry.

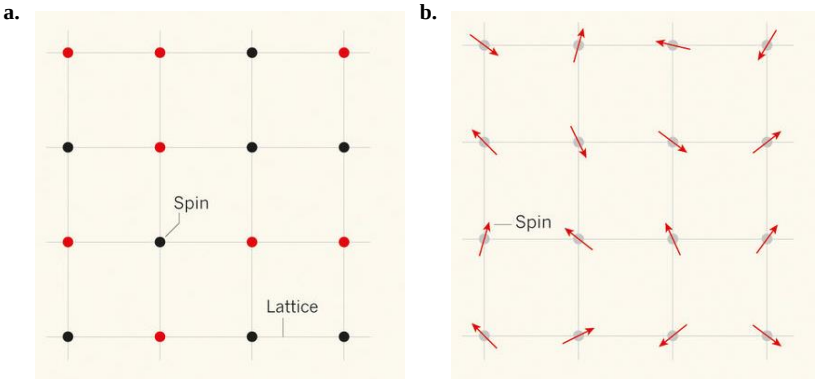

Figure 1.1. **Models of 2D Magnetism.** **a)** Ising two dimensional square lattice, with discrete spins of +/- 1 (red vs black) at each lattice site. **b)** Isotropic Heisenberg two dimensional square lattice, with spins at each site represented by a vector (red arrows). Reprinted with permission from [4].

Two simplified models, the Ising model and the Heisenberg model, have provided the primary means to study the existence and nature of phase transitions within a mathematically tractable framework[7]. These two models are readily applied to magnetic systems. In the case of a ferromagnetic material described by the Ising model, the spins of the magnetic atoms are considered as discrete variables arranged at the vertices of a lattice in 1, 2, or 3 dimensions. Figure 1.1a shows spins arranged on a 2D square lattice[8]. In this model, the spins, σ_i where i represents a particular lattice site, can take on one of two discrete values:

$$\sigma_i = \pm 1$$

Representing spin up or down, respectively. In figure 1a, this is denoted by a red dot (spin up) or a black dot (spin down). Spins on adjacent sites i and j also interact through an exchange interaction, characterized by a constant J_{ij} which can be either positive, favoring a parallel spin alignment, or negative, favoring antiparallel alignment. A spin configuration s corresponds to assigning a specific spin value to every lattice site. In this model, the Hamiltonian is given by[7,3]:

$$H(s) = -\sum_{<i,j>} J_{ij}\sigma_i\sigma_j - \mu\sum_j h_j\sigma_j$$

for a particular spin configuration s, in an external field h.

In addition to providing a mathematical model describing the spins of certain magnetic materials, it also provides a framework within which to study the phase transition of the system and its behavior around the critical point. It was shown rigorously by Ising that for a 1D system there is no phase transition and therefore no long-range magnetic order at temperatures greater than 0K[6,3]. However, for the 2D Ising model, spontaneous magnetization can occur at a non-zero T_c, and the magnetization has the following dependence on temperature:

$$M_0(T) = (1 - T_c/T)^{\beta}$$

With the critical exponent β = ⅛. This relation has been rigorously shown to hold not only for a square lattice but for 2D lattices in general[3]. Spontaneous magnetization can also occur in the 3D case with β = 0.326. This means that for magnetic materials well described by the Ising model, spontaneous magnetic order can exist even in the two dimensional case.

However, a crucial assumption of the Ising model is that the spins at each lattice site have discrete values, +/- 1. Physically, this corresponds to the presence of strong anisotropy in the system such that magnetization essentially can only occur along a specific "easy" axis. For materials with little to no magnetic anisotropy, the more complicated Heisenberg model is more appropriate. In this model, the spins of magnetic atoms are represented by a vector located at each point in the lattice (Fig. 1.1b), rather than a discrete variable with two well defined values. Now, the spins of the magnetic atoms are free to point in any direction. In this picture, the Hamiltonian without an external magnetic field becomes[7]:

$$H = -\frac{1}{2}\sum_{<i,j>} J_{i,j}\hat{S}_i \cdot \hat{S}_j - \mu \sum_j h_j \hat{S}_j$$

Where the spin at each lattice site is now described by a spin operator S_i, typically defined as

$$\hat{S} = \begin{pmatrix} S_x \\ S_y \\ S_z \end{pmatrix}$$

In the Cartesian basis, where S_x, S_y, and S_z are given by the Pauli matrices:

$$S_x = \frac{1}{\sqrt{2}}\begin{pmatrix} 0 & 1 & 0 \\ 1 & 0 & 1 \\ 0 & 1 & 0 \end{pmatrix}, S_y = \frac{1}{\sqrt{2i}}\begin{pmatrix} 0 & 1 & 0 \\ -1 & 0 & 1 \\ 0 & -1 & 0 \end{pmatrix}, S_z = \begin{pmatrix} 1 & 0 & 0 \\ 0 & 0 & 0 \\ 0 & 0 & -1 \end{pmatrix}$$

Like in the Ising model, spins on different lattice sites interact with each other through an exchange interaction, characterized by the exchange constant J. $J < 0$ represents antiparallel spin alignment, while $J > 0$ represents parallel spin alignment.

For systems with continuous symmetry such as those obeying the isotropic Heisenberg model however, it has been rigorously shown by Mermin and Wagner that there can be no spontaneous symmetry breaking in dimensions lower than 3, for sufficiently short-range interactions (i.e., the exchange interaction between nearest-neighbor spins)[9,10]. This means that there can be no spontaneous magnetic order, either ferromagnetic or antiferromagnetic, for dimensions lower than 3 in systems described by the Heisenberg model. In their 1966 paper, they show that for 1 and 2 dimensions respectively, the magnetization in the infinite-volume limit behaves as

$$(1)\ |s_z| < \frac{const.}{T^{\frac{1}{2}}} \frac{1}{|\ln |h||^{\frac{1}{2}}}$$

$$(2)\ |s_z h| < \frac{const.}{T^{\frac{2}{3}}} |h|^{\frac{1}{3}}$$

Which can only show non-zero spontaneous magnetization at 0K[9]. At temperatures above 0K, fluctuations become significant in the low dimensional limit and destroy any long-range magnetic order in 1 and 2 dimensional Heisenberg systems. Spontaneous magnetic order can only occur in the isotropic three dimensional Heisenberg model, and the behavior as a function of T near Tc is given by

$$M_0(T) = (T - T_c)^{0.3689}$$

Therefore, the presence of substantial anisotropy is an essential requirement in order to realize magnetic behavior in low dimensional systems[7].

1.2 Experimental Work: Thin Films

The initial attempts to realize two dimensional magnetic systems experimentally began several decades after this theoretical work. Significant advances in thin film growth such as the

development of ultra-high vacuum (UHV) deposition techniques and molecular beam epitaxy (MBE) enabled layer-by-layer epitaxial growth as well as in-situ characterization. As a result, most initial efforts focused on creating the thinnest possible films and structures using well known 3D magnetic materials such as iron, nickel, and cobalt.

During the 1980's and 1990's, a variety of studies successfully prepared magnetic films ranging from a few monolayers down to sub-monolayer coverage on single crystal substrates. Rau *et al.* successfully grew films of Vanadium on Ag(100) single crystal substrates ranging from 1-7 layers thick using UHV e-beam evaporation onto atomically flat and clean substrates[11]. Li and Baberschke reported the growth of Ni(111) films on W(110) ranging from 2-20 monolayers[12] and Ballantine *et al.* reported growth of p(1x1)-Ni on Cu(111), both using UHV electron-beam epitaxial growth techniques[13]. Huang *et al.* reported the growth of Co, Ni, and Co-Ni alloys on Cu(100) and Cu(111) ranging from 2-20 monolayers, grown using MBE[14].

All of the above studies used in-situ characterization techniques to measure the magnetization of the films as a function of temperature, and quantified the behavior in terms of the critical exponent β in order to monitor the dimensionality of the system. Rau *et al.* used electron capture spectroscopy (ECS) to measure ferromagnetic ordering in their few-layer V films below a Tc of about 300K depending on film thickness. For 5 ML thick films, they observed ferromagnetism of the topmost layer, with $\beta = 0.128$, in close agreement with the theoretical value of 0.125 predicted for a 2D system obeying the Ising model[11]. Both Li and Baberschke and Ballentine *et al.* observe a shift from 3D to 2D behavior in their Ni films. Ballentine *et al.* use the magneto-optical Kerr effect to characterize the magnetization as a function of temperature, however they obtain a value of 0.24 for beta for films in the 2-3 ML range, increasing to 0.32 for an 8 ML film. This is inconsistent with the value for a 2D Ising system, however consistent with

the value obtained for p(1x1) Fe on Au(100)[13]. Li and Baberschke characterized the magnetization of their Ni(111) films using ferromagnetic resonance, and measured a clear transition in the critical exponent from 0.38 for bulk samples roughly consistent for a 3D Heisenberg system, to 0.32 for 15-6 ML thick films (consistent with a 3D Ising system), to 0.13 for <6 ML thick films[12]. Their results clearly demonstrate a change from a Heisenberg to an Ising-type system, followed by a sharp change in critical exponent as the dimensionality of the system crosses from 3 to 2, at around 6 ML. Huang *et al.* also use the magneto-optical Kerr effect to characterize their Ni and Co films, and show a shift in β from about 0.4 for films thicker than 15 ML characteristic of 3D Heisenberg behavior, to 0.23 for films thinner than 6 ML which is typical of systems obeying the 2D XY model[14].

While these studies all observed ferromagnetism in a two-dimensional system, there is significant variation between the results obtained for different studies, even for the same material. Furthermore, because the materials chosen for these studies are three-dimensional crystals, dangling bonds and interface effects also become increasingly dominant as the film thickness is decreased, and can completely overwhelm any well-known bulk behavior. As a result, while all the materials used have well characterized magnetic behavior in their bulk forms, the persistence of magnetism observed as the film thickness decreases could result from magnetic anisotropy introduced from interface effects or reduction of symmetry as the film approaches the single monolayer limit. This is clear from the fact that for all systems characterized, the bulk critical exponent indicates 3D Heisenberg-like behavior. There can be no two-dimensional Heisenberg ferromagnet and a shift to Ising-like or XY-like behavior is observed in all thin-film systems that have successfully demonstrated a transition to two dimensional behavior. Since the magnetic material itself has not changed, the additional anisotropy present in Ising-type systems must have

been introduced externally through sample geometry or sample-specific effects. While these studies were able to observe ferromagnetism in two-dimensional systems, the sample-specific nature of the magnetism makes it virtually impossible to build on the results or incorporate the low dimensional magnets into heterostructures and devices. This highlights the need for a material with strong enough magnetic anisotropy as an intrinsic material property to demonstrate magnetic behavior in the 2D limit without relying on the creation of interfaces or surface effects.

1.3 Experimental Work: van der Waals Crystals

An entirely different approach involves finding magnetic materials with a highly anisotropic layered crystal structure that could potentially approximate a two-dimensional system even in their bulk forms. This was the subject of research as early as 1969 on the layered perovskite K_2NiF_4, and isostructural Rb_2MnF_4 and Rb_2FeF_4[15,16]. Using neutron diffraction, Birgeneau *et al.* showed that between about 200K and the Neel temperature of 97K, very long range correlations existed indicative of magnetic ordering within the quasi-two-dimensional NiF planes, with no measurable correlations between planes. Even though the system showed a sharp transition to 3D ordering at 97.5K, scattering peaks aside from the expected 3D Bragg diffraction peaks appeared to be entirely 2D in nature. Furthermore, the sublattice magnetization was shown to vary as $(1 - \frac{97.5}{T})^{\beta}$ with a β of 0.15[16]. This strongly suggests that the antiferromagnetic intra-layer magnetization remains two-dimensional in nature. However, the presence of three-dimensional order below the critical temperature in these bulk crystals, regardless of their structural anisotropy, complicates any investigation of low dimensional magnetism.

This approach has been revisited, in light of recent success exfoliating similarly layered crystals such as graphene and the well-known MX_2 semiconductors to their two-dimensional

monolayer limit[17–19]. Exfoliating these layered magnetic materials could also remove complications from the presence of three-dimensional magnetic order below the critical temperature, such as was seen in the early studies of K_2NiF_4 perovskites. Furthermore, weak interlayer interactions and a lack of dangling bonds suggest the possibility of observing two dimensional magnetism due entirely to the layered magnetic material itself.

Numerous van der Waals crystals exist that show magnetic properties in their bulk forms. These include $CrXTe_3$ (X=Si, Ge)[20,4,21], $RuCl_3$[22–24], APB_3 (A=Fe, Mn, and B=S, Se)[25,26], and CrX_3 (X=Br, F, I, Cl)[27–31], among others. Theoretical studies have also predicted that several of the compounds should retain their magnetic properties down to the few-layer or monolayer limit. $CrXTe_3$ and APB_3 are predicted to be anti-ferromagnetic (AFM) at monolayer limit[21,26]. Calculations also show bilayer $MnPSe_3$ has electrically tunable magneto-optical effects by breaking combined time-reversal and inversion symmetry[32].

Recent experimental studies have successfully exfoliated several layered van der Waals magnets, and have shown signs of magnetism persisting to the few-layer or even monolayer limit. Wang *et al.* and Lee *et al.* demonstrated signs of Ising-type antiferromagnetic order in monolayer $FePS_3$ flakes by monitoring Raman peaks sensitive to symmetry breaking or magneto-structural changes while cooling through the transition temperature of $FePS_3$[33,34]. Lee *et al.* also show that the transition temperature is virtually independent of flake thickness. This is in strong contrast to thin-film magnets, where the transition temperature typically decreases significantly with film thickness, and implies that interlayer and substrate interactions are weak and that any magnetic behavior observed in the monolayer limit results from the intrinsically two dimensional nature of the magnetism in $FePS_3$. However, these studies used Raman scattering to indirectly measure the

magnetism in $FePS_3$, and inferred coupling between the observed Raman modes and magnetic ordering based on the behavior of the Raman peaks at the Neel temperature.

Gong *et al.* used magneto-optical Kerr effect measurements to directly measure the magnetic behavior of $CrGeTe_3$ flakes exfoliated down to bilayer thickness[35]. They observed ferromagnetic behavior with small but non-zero remanant magnetization (signal at 0T equivalent to 2% of saturation) and a Curie temperature of 10K for 6-layer flakes (compared to the bulk Curie temperature of ~35K) suggesting the presence of very small magnetocrystalline anisotropy. However, flakes thinner than three layers showed no remnant magnetization and a Curie temperature postulated to be below the lower limit of their cryostat. Applying a small external field enabled significant modulation of the Curie temperature, suggesting that while the extremely small magnetic anisotropy of CGT prevented observation of intrinsic ferromagnetism in few-layer flakes, the application of even tiny external fields effectively supplied enough anisotropy externally to observe ferromagnetic behavior.

Among these material systems, the CrX_3 family is particularly promising since these compounds are predicted to be ferromagnetic (FM) semiconductors in the monolayer limit[28–31]. FM semiconductors are intriguing for technological applications, as they combine semiconducting properties necessary for logic circuits and magnetic properties ideal for spintronics[1]. Furthermore, many of the CrX_3 compounds are predicted to have very high magnetocrystalline anisotropy, making them ideal candidates for realizing low dimensional magnets[30,31]. So far, despite several recent theoretical works on the possible 2D magnetic properties of CrX_3 materials, the experimental investigation of CrX_3 has been sporadic and no studies have investigated few-layer flakes. The following two chapters discuss the isolation, characterization, and electrical control, of magnetic properties in few-layer flakes of CrI_3.

Chapter 2. MAGNETISM IN ATOMICALLY THIN CrI_3

In this chapter I describe the structure and magnetic properties of atomically thin flakes of CrI_3. After discussing the magnetic properties of bulk CrI_3 crystals, I describe the methods we used to exfoliate these bulk crystals down to monolayer limit and our optical characterization technique based on the magneto-optical Kerr effect. Using this technique, we characterize the magnetic behavior in monolayer, bilayer, and other few-layer CrI_3 flakes, identifying the first intrinsic two-dimensional magnetic material.

2.1 Bulk CrI_3: Crystal Structure and Magnetic Properties

The CrX_3 compounds (where X is a halide atom Cl, Br, or I) have been studied sporadically since the 1950's, since they are one of the few intrinsically ferromagnetic materials that also show insulating or semiconducting behavior[27]. Initial studies of CrI_3 in particular focused on crystal growth and preliminary structural characterization using x-ray diffraction. The structure of CrI_3 was reported to coincide with that of $CrCl_3$, and to belong to the D33 space group[27,36]. Later studies began to investigate the magnetic and optical properties of polycrystalline CrI_3 powder samples, demonstrating ferromagnetic behavior below a measured Curie temperature of 68K, and spontaneous magnetization along an axis perpendicular to the basal plane[28,37]. However, the properties of CrI_3 and the other CrX_3 compounds remained largely unexplored beyond initial characterization.

Following the successful isolation of graphene and other atomically thin materials, the CrX_3 compounds and CrI_3 in particular have become a focus of recent interest. Theoretical studies by Zhang *et al.* and Wang *et al*. predict ferromagnetic coupling both intra-layer and interlayer, with an easy axis oriented perpendicular to the layer plane even down to the monolayer limit[30,31].

Importantly, Zhang *et al*. predict that the CrX_3 compounds have a low cleavage energy, and should exfoliate easily to few or monolayer limit[30]. Furthermore, CrI_3 is predicted to show very strong magneto-crystalline anisotropy (686 μeV /Cr vs 186 μeV/Cr for $CrBr_3$ and 32 μeV/Cr for $CrCl_3$)[30]. This is promising, since the presence of strong magnetic anisotropy is essential in order to retain intrinsic magnetic properties to the two dimensional limit (see section 1.1). A recent study by McGuire *et al.* reports detailed temperature-dependent structural characterization and magnetic behavior, providing the first measurements of single crystal bulk CrI_3[29].

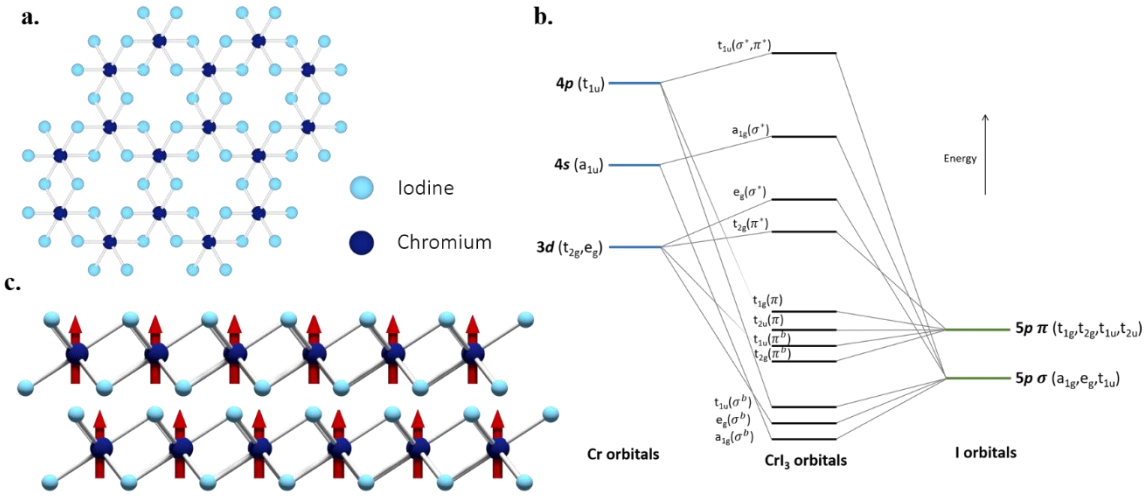

Figure 2.1. **Bonding and structure of bulk CrI_3. a)** Monolayer CrI_3 crystal structure, showing octahedral coordination of the central Cr^{3+} ions (dark blue spheres) by six I^- anions (light blue spheres). **b)** Molecular orbital diagram for CrI_3. **c)** Ferromagnetic intra-layer and inter-layer coupling in CrI_3.

Within each layer, Cr^{3+} ions are arranged in a hexagonal honeycomb lattice. Each Cr ion is coordinated to six X^- ions in edge sharing octahedra, while each X^- ion is in turn shared between two Cr ions. Figure 2.1a shows the octahedral coordination within a single layer of CrI_3, as viewed

from above the layer. Within the bulk crystal, the layers stack in approximately A-B-C stacking order[29].

Molecular orbital theory and ligand field theory provide a more detailed picture of the orbitals involved in bonding within each CrI_3 layer, and the behavior of the Cr^{3+} valence electrons. Figure 2.1b shows the molecular orbital diagram for CrI_3, taking into account the 5p iodine valence electrons and 3d, 4s and 4p chromium valence electrons, in an octahedral ligand field provided by the six I^- ions[38]. The Cr $3d^3$ electrons occupy the antibonding t_{2g}^* orbital, and magnetic properties are dictated by the interaction and resulting orientation of these three unpaired spins[38]. Considering nearest-neighbor interactions only, the magnetic behavior is thought to result from a competition primarily between the direct exchange of Cr-Cr sites and superexchange interaction mediated by an iodine anion. The direct Cr-Cr exchange interaction is antiferromagnetic. However the superexchange interaction mediated by an iodine anion through the Cr-I-Cr bond is ferromagnetic, as a result of the near 90° bond angle[39]. The CrI_3 octahedra are slightly distorted, with a bond angle of 95.4° however. This leads to an increased Cr-Cr separation of 4.05Å. While the change in the bond angle does not greatly alter the nature of the superexchange interaction, the increased distance between Cr^{3+} ions reduces the significance of the direct exchange interaction towards the overall magnetic behavior. The result is that the ferromagnetic superexchange interaction dominates the antiferromagnetic direct exchange interaction, and CrI_3 is predicted to order ferromagnetically within each layer[30]. Figure 2.1c shows the ferromagnetic alignment of spins in each layer of CrI_3, as well as the predicted ferromagnetic interlayer coupling.

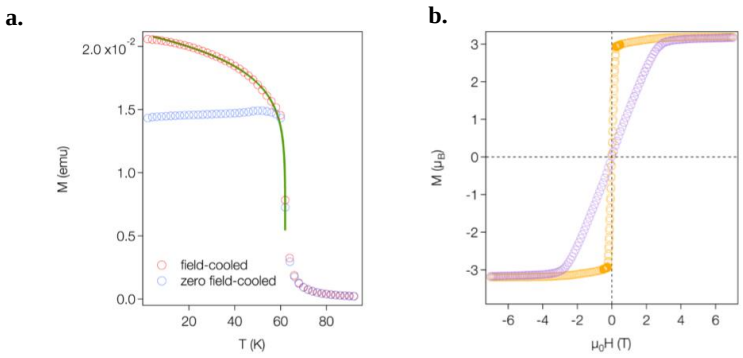

Figure 2.2. **Magnetic behavior of bulk CrI_3. a)** Zero-Field Cooled/Field-Cooled measurements with a criticality fit showing $\beta = 0.125$. **b)** Magnetization m (μ_b/Cr) vs H (Tesla) for fields applied perpendicular and parallel to the c-axis of the crystal measured in a).

This is consistent with characterizations of magnetism in bulk CrI_3. Both in early reports and the recent study by McGuire *et al*., ferromagnetic behavior is reported with a Curie temperature of around 60K, and an easy axis oriented perpendicular to the basal plane[29,37]. Figure 2.2a shows zero-field cooled/field-cooled temperature dependence of the magnetization of a CrI_3 bulk crystal measured using a SQUID magnetometer. Both temperature dependent curves were taken in a field of 10G applied perpendicular to the basal plane. The divergence in magnetization at ~60k, suggests ferromagnetic behavior with a Curie temperature of 60K. Figure 2.2b shows magnetization vs applied field, for fields ranging from 6.5T to -6.5T, applied parallel and perpendicular to the c-axis of the crystal. When the field is applied along the c-axis, the magnetization jumps sharply to its saturation value, close to 3 μ_b /Cr. When the field is applied perpendicular to the c axis, the magnetization gradually increases to its saturation value as the applied field is increased up to 10's of kOe[40]. This directionality of the magnetization implies an

easy axis lying parallel to the c-axis, and a significant anisotropy field of 30 kOe consistent with predictions by Zhang *et al*[30].

Figure 2.2a also shows a criticality fit of the data (green line) ie $M(T) \sim \left(1 - \frac{Tc}{T}\right)^{\beta}$ with $\beta = 0.125$ and Tc = 61K. The close agreement between the criticality fit for a 2D Ising system and the experimental data indicates that even in the bulk crystals, the magnetic behavior of CrI_3 is largely two dimensional in nature and is consistent with the Ising model[40].

2.2 Exfoliating and Identifying Few-Layer CrI_3

Bulk CrI_3 can be exfoliated using the scotch tape method, similar to other layered van der Waals materials. Figure 2.3a shows a CrI_3 flake of varying thickness exfoliated from a bulk crystal onto a 285 nm SiO_2 substrate. A pervasive challenge associated with studying exfoliated CrI_3 flakes however, is their strong sensitivity to moisture. All exfoliation and sample preparation must be carried out in a glovebox under inert atmosphere (either Ar or N_2), in order to prevent immediate degradation of the flakes. As a result, it is impossible to assign the thickness of as-exfoliated flakes directly using atomic force microscopy (AFM). Instead, thickness is assigned based on quantitative optical contrast, obtained from the RGB value of pixels in an optical microscope image of the target flake. This method has been used successfully for a range of other exfoliated materials on SiO_2 substrates, including graphene and MX_2 semiconductors. For the experiments detailed here, CrI_3 flakes were exfoliated onto 285nm SiO_2 on Si.

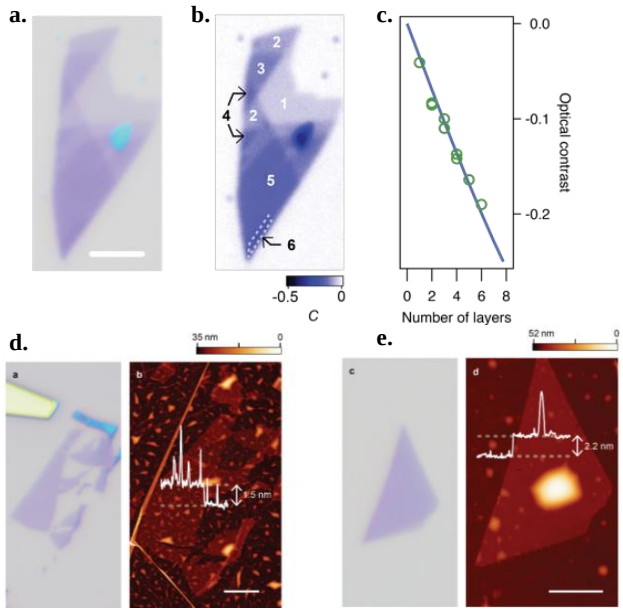

Figure 2.3. **Optical contrast of CrI_3 flakes. a)** Image of CrI_3 flake on 285 nm SiO_2 (scale bar is 5 μm). **b)** Optical contrast and layer assignment for each region on the flake in a). **c)** Normalized optical contrast vs layer number for monolayer to 6-layer flakes. **d)** Image and AFM image of a bilayer flake, showing a height of 1.5 nm. **e)** Optical microscope image and AFM image of a trilayer flake, showing a 2.2 nm flake height.

In the case of exfoliation onto 285 nm SiO_2, optical microscope images are taken under monochromatic illumination using a 631nm band pass filter. The R-channel value from the RGB value of each pixel is extracted and averaged over each flake and substrate region to give the reflected intensities of the flake and substrate. Figure 2.3b shows an image of the optical contrast for the same flake shown in figure 2.3a, with the corresponding layer number for each region. For few layer flakes, optical contrast increases linearly vs layer number and can be used to quantitatively assign layer number. Figure 2.3c shows a plot of normalized optical contrast vs layer number for few-layer CrI_3 flakes and a linear fit to the data (blue line).

In order to unequivocally establish the correct correspondence between layer number and optical contrast, bi-layer and tri-layer CrI_3 flakes were encapsulated in graphite inside an argon glovebox and removed for AFM measurements in ambient conditions. Figure 2.3d and e show side by side optical and AFM images of bilayer and trilayer CrI_3 flakes respectively, together with a line cut across each flake. The bilayer flake shows a step-height of 1.5 nm, while the trilayer flake has a thickness of 2.2 nm. This allows the monolayer height to be inferred as 0.7 nm, in good agreement with predictions based on bond length[30,40]. From the optical contrast values of the flakes used for AFM, we are able to accurately calibrate our layer number vs optical contrast assignment.

2.3 Optical Characterization

To characterize the magnetic behavior of CrI_3 flakes ranging from monolayer to 10's of nm in thickness, the magneto-optical Kerr effect is used to non-destructively measure the magnetization of the flakes. The magneto-optical Kerr effect (MOKE) describes the rotation of plane-polarized light upon reflection from the surface of a magnetic material. Similar to the Faraday Effect seen in the case of a polarized beam transmitting through a magnetic material, a linearly polarized beam reflected off of the surface of a magnetic material will undergo a rotation through some angle, θ_k known as the Kerr angle. This effect arises from the magnetic circular birefringence induced when a sample gains a non-zero magnetization M, which causes a phase difference between right-circularly polarized light (RCP) and left-circularly polarized light (LCP) both upon reflection from and transmission through the medium[41]. This phase difference between RCP and LCP upon reflection from the magnetic material will lead to an observed rotation in the linear polarization of the reflected and transmitted beams, through an angle θ_k

Upon magnetization, the Fresnel coefficients $\hat{r}_+$ and $\hat{r}_-$ for RCP and LCP respectively given by

$$\hat{r}_+ = r_+ e^{i\theta_+}$$

$$\hat{r}_- = r_- e^{i\theta_-}$$

are no longer identical. The Kerr rotation is determined from the phase shift between the two Fresnel coefficients as[41]

$$\Delta\theta = \theta_+ - \theta_-$$

$$\theta_k = -\frac{1}{2}\Delta\theta$$

The Fresnel coefficients are related to the magnetization of the material through the off diagonal elements of the dielectric tensor:

$$\varepsilon = \begin{pmatrix} \widetilde{\varepsilon_{xx}} & iQM & 0 \\ -iQM & \widetilde{\varepsilon_{xx}} & 0 \\ 0 & 0 & \widetilde{\varepsilon_{zz}} \end{pmatrix}$$

Where M is the magnetization along the $\hat{z}$ direction and Q is the complex Voigt constant. From this expression for the dielectric tensor, the indices of refraction for right and left circularly polarized light are

$$\widetilde{n_\pm} = \sqrt{(\widetilde{\varepsilon_{xx}} \pm QM)}$$

And the Fresnel coefficients are given by[42]

$$\widetilde{r_\pm} = \frac{1-\tilde{n}_\pm}{1+\tilde{n}_\pm},$$

A change in magnetization state of the sample along $\hat{z}$ will manifest as a change in the refractive index seen by incident RCP vs LCP light. This in turn leads to different Fresnel coefficients for the different polarizations, and a resulting phase difference between RCP and LCP light reflected off the surface of the sample at 90° incidence, proportional to the magnetization of the sample[42].

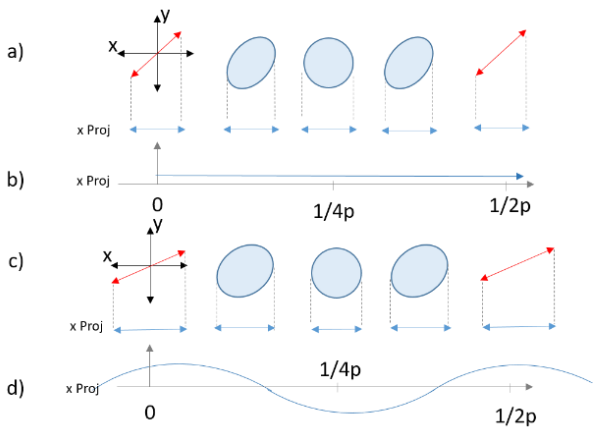

Figure 2.4. **Polarization modulation by PEM. a)** Polarization state of light as a function of frequency, with no Kerr rotation. **b)** X-projection of the polarization in a). **c)** Effect of Kerr rotation on the polarization of light leaving the PEM. **d)** X-projection of the polarization in c).

In order to practically measure the MOKE signal of few layer CrI_3 flakes, we use an AC polarization modulation technique with lock-in detection described by Sato *et al.*, allowing detection of signals as low as 100 μrad[41]. A photo-elastic modulator (PEM) is used modulate the polarization state of incident linearly polarized light, by varying retardation along the fast axis of the PEM (Fig. 2.4 a-d). Figure 2.4a shows the resulting polarization state of light incident 45° to the PEM fast axis, over a half modulation period. At 1/4p, the linearly polarized light becomes circularly polarized, while at 0 and 1/2p the light passes through the PEM unchanged. At all other points the light is elliptically polarized. Without any added Kerr rotation, the projection of the polarization modulated beam onto the PEM slow axis (x-axis) remains constant (Fig. 2.4b). However, any added Kerr rotation can be observed at all points not perfectly circularly polarized, as a deviation in magnitude of the x-projection of the light (Fig. 2.4c and d). Lock-in detection at 1/2p (twice the fundamental frequency of the PEM) therefore allows observation of any Kerr

rotation, manifest as a change in intensity of the x-projection of light reflected from the sample surface[41].

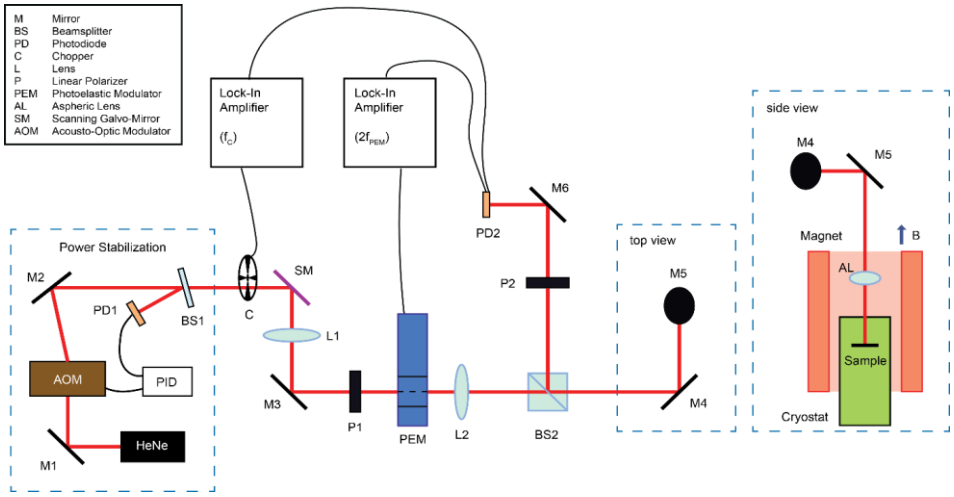

Figure 2.5. **Schematic of optical setup.**

Figure 2.5 shows a cartoon of the experimental setup used to measure the Kerr rotation of few-layer CrI_3 flakes. Emission from a HeNe laser at 633 nm is power stabilized using an AOM and servo-control feedback loop, passes through a mechanical chopper, and is then polarized 45 degrees to the fast axis of the photo-elastic modulator (PEM). Passing through the PEM, the beam is sinusoidally phase modulated at 50.1 kHz. The polarization modulated beam is then focused onto the surface of the CrI_3 flakes at normal incidence using a 5mm aspheric lens. The CrI_3 flakes on SiO_2/Si wafers are held in a closed cycle optical cryostat, maintained at a base temperature of 15k unless otherwise specified. An external magnetic field is applied using a superconducting solenoid magnet at fields up to +/- 2.5 T, allowing observation of θ_K as a function of external field. The reflected light is collected by the same aspheric lens and separated from the incident beam by a laser-line non-polarizing beam splitter cube. An analyzer projects the reflected beam onto the PEM slow axis (x axis in figure 2.4), and the intensity of the analyzed beam is detected using an amplified photodiode. Two lock-in amplifiers are used, one detecting the photodiode signal at

twice the PEM frequency (1/2p in figure 2.4), and one detecting the reflected intensity at the frequency of the mechanical chopper. The Kerr rotation signal is obtained from the ratio of these two signals, providing a Kerr rotation measurement independent of fluctuations in laser power or variations in the intensity of the reflected beam.

2.4 Magnetism in Monolayer CrI_3

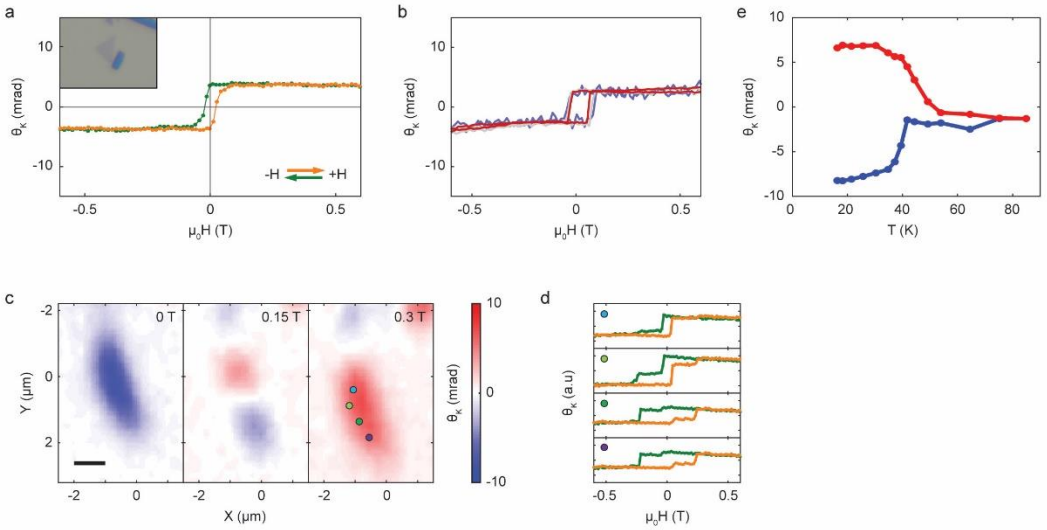

Figure 2.6. **Magnetism in monolayer flakes.** **a)** MOKE signal for a CrI_3 monolayer. The inset shows an optical image of an isolated monolayer (the scale bar is 2 μm). **b)** Power dependence of the MOKE signal. **c)** MOKE maps at $\mu_0 H$ = 0 T, 0.15 T and 0.3 T on a different monolayer. The scale bar is 1 μm. **d)** θ_K versus $\mu_0 H$ sweeps taken at four points marked by dots on the $\mu_0 H$ = 0.3 T map in **c**. **e)** Temperature dependence of MOKE signal with the sample initially cooled at $\mu_0 H$ = 0 T (blue) and 0.15 T (red).

Figure 2.6a shows θ_K as a function of $\mu_o H$ for a monolayer CrI_3 flake shown in Figure 2.6a inset. A single hysteresis loop in θ_K centered around $\mu_o H = 0$ T, with a small but nonzero remnant Kerr rotation, demonstrates out-of-plane spin polarization. This implies that monolayer CrI_3 shows Ising ferromagnetism, since it has retained the ferromagnetic behavior of the bulk crystal in the 2D limit. Figure 2.6b shows power dependence of θ_K as a function of external field, for 3 μW (blue line), 10 μW (pink line) and 30 μW (red line). The curves overlap exactly, indicating that the magnetization is independent of the excitation power. Aside from power dependent measurements, all measurements were taken with an excitation power of 10 μW. For a total of 12 monolayer samples measured, all show similar MOKE behavior with consistent remanent θ_K values of about 5 ± 2 mrad at $\mu_o H = 0$ T. The coercive field ($\mu_o H_c$), which is ~50 mT for the sample in Fig. 2.6a, can vary between samples due to the formation of domain structures in some samples.

Figure 2.6c shows spatial maps of θ_K for a different monolayer, taken at increasing magnetic field values. After cooling the sample from above T_c at $\mu_o H = 0$ T, the entire monolayer is spontaneously magnetized (defined as spin down, blue) corresponding to a uniform negative θ_K depicted in the first panel. As the field is increased to 0.15 T, the magnetization in the upper half of the flake switches direction (now spin up, red). As the field is further increased to 0.3 T, the lower half of the monolayer flips and the entire flake becomes spin up, parallel to $\mu_o H$. This observation of micron-scale lateral domains suggests different values of coercivity in each domain. Magnetic field sweeps (θ_K vs $\mu_o H$) taken at discrete points ranging across both domains (Fig. 2.6d) show the difference in coercive field between the upper and lower half of the monolayer. Sweeps taken only on the upper domain, marked by a blue circle, show a much narrower hysteresis loop (about 50 mT) than sweeps from spots on the lower domain (orange and purple circles, about 200 mT). When the beam spot is centered between the two domains, contributions from both can be

seen in the resulting hysteresis loop (green circle), a consequence of the ~1 μm beam spot illuminating both domains.

To determine the monolayer T_c, we measured the irreversible field cooled (FC) and zero-field cooled (ZFC) Kerr signal. ZFC sweeps were performed by cooling the sample in zero field and measuring θ_K while warming in a small magnetic field ($\mu_o H$ = 0.15 T). Following the disappearance of any Kerr signal or domain at a temperature well above T_c (90 K), the sample is cooled back down in the presence of the same external magnetic field. Thermomagnetic irreversibility can be observed below T_c, at which point the ZFC sweep and the FC sweep diverge as illustrated in Fig. 2.6e. We measured the average T_c for the monolayer samples to be 45 K, slightly lower than the value (61 K) for bulk samples.

2.5 Layer-Dependent Magnetism in Bilayer and Few-Layer CrI_3

The layered structure of CrI_3 provides a unique opportunity to investigate interlayer coupling in few-layer flakes, and its potential effect on the observed magnetic behavior and Curie Temperature as a function of layer number. Figures 2.7a and b show θ_K vs $\mu_o H$ for representative 1 and 2 layer CrI_3 samples. All measured monolayer samples consistently show ferromagnetic behavior with a single hysteresis loop centered at $\mu_o H$ = 0 T. For trilayers and thin bulk samples, T_c is consistent with the bulk value of 61 K. The relatively small decrease of T_c from bulk to few-layer and monolayer samples suggests that interlayer interactions do not dominate the ferromagnetic ordering in CrI_3. Compared with magnetic thin films whose magnetic properties strongly depend on the underlying substrate, the weak layer-dependent T_c also implies a negligible substrate effect on the ferromagnetic phenomena in atomically-thin CrI_3. As a result, exfoliated CrI_3 of all thicknesses can be regarded as isolated single crystals.

A further observation is that bilayer CrI_3 shows a markedly different magnetic behavior (Fig. 2.7b). For all bilayer samples measured, the MOKE signal is strongly suppressed, with θ_K near zero (subject to slight variation between samples) at field values between about ±0.65 T. This observation implies a compensation of the out-of-plane magnetization. Upon crossing a critical field, θ_K shows a sharp jump, depicting a sudden recovery of the out-of-plane spin-aligned orientation of the two layers. This new magnetic state has an order of magnitude larger saturation θ_K (40 ± 10 mrad) than monolayer samples, and slightly smaller than for trilayers.

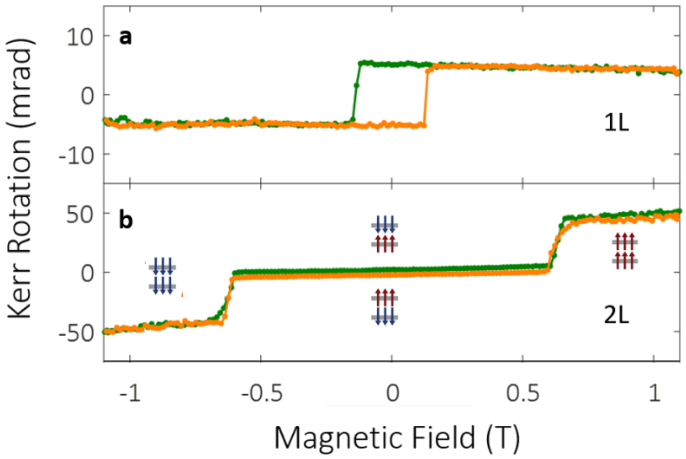

Figure 2.7. **Layer dependent magnetic behavior. a)** MOKE signal on a monolayer (1L) CrI_3 flake. **b)** MOKE signal from a bilayer CrI_3. Insets depict bilayer (2L) magnetic ground states for different applied fields.

The suppression of Kerr signal at zero magnetic field demonstrates that the ground state has zero out-of-plane magnetization. The plateau behavior of the M-H curve further implies that there are no in-plane spin components; otherwise, the M-H curve would show a gradual increase of the MOKE signal with increasing perpendicular magnetic field. Rather, this observation suggests that each individual layer is ferromagnetically ordered (out-of-plane) while the interlayer coupling is antiferromagnetic. In this case, the strength of the interlayer coupling determines the

field at which jumps between different plateaus occur, around ±0.65 T. The detailed mechanism of this coupling is still unknown. Another bilayer feature distinct from that of the monolayers is the vanishingly small hysteresis around the jumps, suggesting negligible net perpendicular anisotropy. A possible interpretation is that the shape anisotropy (which prefers in-plane spin orientation) nearly compensates the intrinsic magnetocrystalline anisotropy (which prefers out-of-plane spin orientation) so that the overall anisotropy is close to zero.

The insets in Fig. 2.7b display the layer-by-layer switching behavior that leads to plausible magnetic ground states of bilayer CrI_3. When the magnetic field is within ±0.65 T, the magnetization of the two layers are oppositely oriented to one another. Thus, the net magnetization vanishes and bilayer CrI_3 behaves as an antiferromagnet with an exchange field of about 0.65 T. When $|\mu_o H| > 0.65$ T, magnetization in one layer flips to align with the external magnetic field and restores out-of-plane magnetization, giving rise to the large MOKE signal. At around $|\mu_o H| = 0.65$ T, the MOKE signal sharply increases from near zero to its saturation value within about 100 mT, suggesting an abrupt increase of out-of-plane magnetization by a small change of magnetic field. Such behavior is indicative of metamagnetism, the magnetic field-driven transition from antiferromagnetic ordering to a fully spin-polarized state.

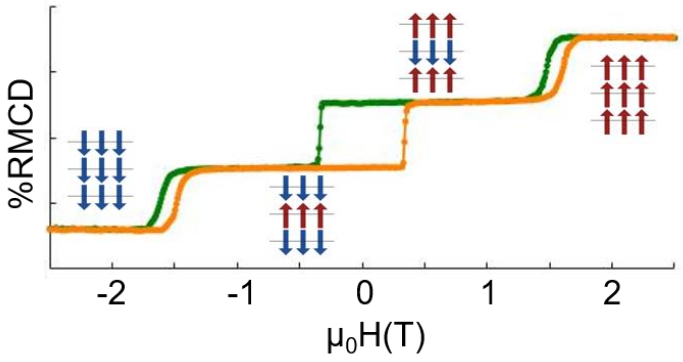

Figure 2.8. **MOKE signal from a trilayer flake of CrI_3.**

Trilayer CrI_3 flakes also show a distinct layer-dependent magnetic behavior. Figure 2.8 shows θ_K vs field for a representative trilayer flake, with proposed spin configurations for each state, shown as insets in figure 2.8. At large applied magnetic fields either positive or negative ($\mu_o H > |1.5|T$) the trilayer is in the fully spin-aligned state, with all three layers aligned with the external field. As the magnitude of the applied field falls below 1.5T, the middle layer flips orientation leading to antiferromagnetic coupling between all three layers in the trilayer. However, in this configuration there is a non-zero Kerr signal at zero field corresponding to the signal from a single layer, unlike in the case of bilayer flakes where the signals from the two antiferromagnetically coupled layers exactly cancel each other. When the field then decreases (increases) to -0.5T (0.5T), a second layer flips to align with the external field causing a second jump in the Kerr signal. Finally at ±1.5T the third layer flips to align with the external field and the trilayer is in the fully spin-aligned state with the opposite spin orientation. The time reversal of this process is true when the field is swept in the opposite direction. Four-layer and thicker flakes also show unique layer-dependent magnetic behavior. The discrete step-like behavior seen in the several nm thick flake indicates that layer-by-layer flipping is still present as the thickness of the flakes increases beyond several layers. This suggests that while the intra-layer coupling remains strongly ferromagnetic for all layer numbers, the mechanism of interlayer coupling is more nuanced and sensitively depends on the thickness of the flakes.

2.6 Final Remarks

These results indicate that Ising-type ferromagnetism persists in CrI_3 down to monolayer limit. Not only does monolayer CrI_3 show robust ferromagnetism with a coercive field of up to about 0.3 T, but few-layer CrI_3 flakes show distinct interlayer coupling leading to novel layer-dependent magnetic behavior. This highlights the importance of van der Waals materials as a

platform to explore not only truly two-dimensional physics, but also layer dependent phenomena that are inaccessible using any other class of material. Since these 2D magnets are free from dangling bonds and interface effects, this discovery opens the door for further work interfacing them with other 2D materials and integrating them into van der Waals heterostructure devices.

Chapter 3. ELECTRICAL CONTROL OF MAGNETISM IN BILAYER CrI_3

Achieving electrical control of magnetism has long been a goal of condensed matter physics and materials science. It not only addresses fundamental aspects of magnetic phenomena and phase transitions, but also has technological importance for developing electrically coupled spintronic devices, such as voltage-controlled magnetic memories with low operation energy. Building on the initial discovery of intrinsic 2D magnets described in chapter 2, a natural next step is to explore ways to control their magnetic properties electrostatically, furthering understanding of the nature of their magnetic behavior and extending their potential technological relevance.

3.1 Electrical Control of Magnetism in Other Systems

Previous studies of electrically controlled magnetism primarily focused on dilute magnetic semiconductors such as (Ga,Mn)As and (In,Mn)Sb, and metallic thin films[43–45]. Electrical control of magnetic behavior in these two classes of materials arises from very different physical phenomena. In dilute magnetic semiconductors, magnetism is induced in non-magnetic III-V (or other) semiconductors by introducing a high concentration of magnetic dopants, typically manganese. The magnetic properties arising from the introduction of these magnetic dopants are carrier-mediated, meaning that the spins on each magnetic ion interact through charge carriers in the semiconductor, leading to magnetic ordering of the spins below the Curie temperature of the material[46]. In the case of (Ga,Mn)As, the manganese ions act as acceptors, donating holes that mediate a ferromagnetic interaction between the unpaired d-electron spins on the Mn ions[46]. In the absence of holes, there is a weakly antiferromagnetic superexchange interaction between the Mn d-electrons. This carrier-mediated magnetic behavior readily lends itself to electrostatic tuning.

Studies on (InMn)As have shown that changing the hole concentration through electrostatic gating mediates the strength of the ferromagnetic exchange interaction, leading to an observable change in the Curie temperature[44].

Metallic thin films have also shown gate tunable magnetic behavior. In this case, thin films of materials showing itinerant ferromagnetism (FePt and FePd) were selected[43]. In order to overcome the formation of surface charge upon application of an electric field, which would screen penetration of the field into the bulk, the film thickness was kept below 4 nm and an electrolytic double layer was used to generate a large electric field at the surface of the film. In these films, the application of an electric field strongly effects the electron density at the film surface thereby changing the intrinsic magnetic behavior of the metal[43]. Recent work on two-dimensional (2D) magnets has revealed a new system in which to explore the electrical control of magnetic properties.

3.2 Device Fabrication

To explore gate-controlled magnetoelectric effects, we fabricated gated bilayer CrI_3 devices. Bulk crystals of CrI_3 were mechanically exfoliated onto either 285 nm SiO_2/Si substrates for dual-gated devices or the commercially available viscoelastic polymer Gel Film from Gel-Pak. All fabrication using these crystals was performed in a glove box with argon atmosphere to prevent degradation of the flakes upon exposure to moisture. Bilayer flakes were identified by their optical contrast relative to the substrate as described in section 2.2.

Devices were fabricated using an all-dry polymer transfer technique to sequentially pick up the van der Waals layers for the device and deposit them on the required substrate[47]. In this technique, a polymer stamp is fabricated using a poly(bisphenol A carbonate) (PC) film placed over a polydimethylsiloxane square attached to a glass slide. This stamp is then attached to a

micromanipulator arm, integrated with an optical microscope. Once a target flake is identified under the optical microscope, the stamp can then be positioned over the target flake and lowered down onto the substrate until the PC film makes contact with the target flake. The temperature of the substrate is then increased to promote adhesion between the flake and the PC film on the stamp. The temperature is then decreased and the stamp is retracted, picking up the target flake. This process is then repeated to pick up the desired components for the device. In this case, the flakes were picked up sequentially: graphite top gate, top hexagonal boron nitride, graphite contact, bilayer CrI_3, bottom hexagonal boron nitride.

Metallic Cr/Pd contacts on 285 nm SiO_2/Si substrates were prepared using electron beam lithography and poly(methyl methacrylate) resist fabrication followed by deposition of chromium and palladium using electron beam evaporation. Each chip was then fixed to a DIP socket chip carrier with silver paint and wire bonded to the pads of the chip carrier.

The completed dual-gated stacks were transferred on top of the Cr/Pd contacts and released by heating to 170ºC. The non-encapsulated devices were fabricated by transferring the as-exfoliated bilayer CrI_3 flake on Gel Film directly onto the metallic contacts. Finally, each socket was sealed with a glass coverslip using Crystalbond under inert conditions to allow removal from the glovebox for optical measurements.

Devices without a top gate were characterized using MOKE, as described in chapter 2.3. Devices with a top gate were characterized using reflectance magnetic circular dichroism (RMCD), a similar optical technique to characterize magnetic behavior in thin films, using an almost identical optical setup to the one shown in figure 2.5. Materials that exhibit an out-of-plane magnetization, **M**, may display magnetic circular birefringence (MCB) and magnetic circular dichroism (MCD). Both MCB and MCD accrue a difference in the phase and amplitude,

respectively, between right- and left-circularly polarized (RCP, LCP) light that vary as a function of **M**. When linearly polarized light, an equal superposition of RCP and LCP, is normally incident and reflects off the magnetized material, the phase difference between RCP and LCP leads to a rotation of the linear polarization through an angle, θ_K, from the magneto-optical Kerr effect (MOKE) and induces ellipticity through reflective magnetic circular dichroism (RMCD)[41]. Both MOKE and RMCD probe the magnetic behavior of the material through the linear dependence of the off-diagonal elements of the dielectric tensor on the magnetization. In the case of devices fabricated with a top gate, the RMCD signal was used to characterize their magnetic behavior.

Both MOKE and RMCD measurements were performed in a closed-cycle helium cryostat with a base temperature of 15 K. A superconducting magnet allowed fields of up to 7 T in the Faraday geometry to be applied on all devices. The AC lock-in measurement technique used to measure the MOKE and RMCD signal follows the previous characterization of magnetism in exfoliated flakes of CrI_3 described in section 2.3. For RMCD measurements, the analyzing polarizer was removed, and the lock-in frequency was set to the fundamental frequency of the PEM rather than its second harmonic, thereby detecting the circularly polarized component instead of the linearly polarized component.

3.3 Optical Characterization of Gated Devices

The structure of a representative bilayer CrI_3 device is shown in Fig. 3.1b. The device is a vertical structure composed of a bilayer CrI_3 flake and a graphite contact encapsulated between two hexagonal boron nitride (hBN) flakes and a graphite top gate. The hBN flakes protect the bilayer CrI_3 from degradation in ambient conditions and also act as dielectric layers for electrostatic doping through either the graphite top gate or the silicon wafer. Figure 3.1c shows a false-color optical microscope image of a gated bilayer CrI_3 device.

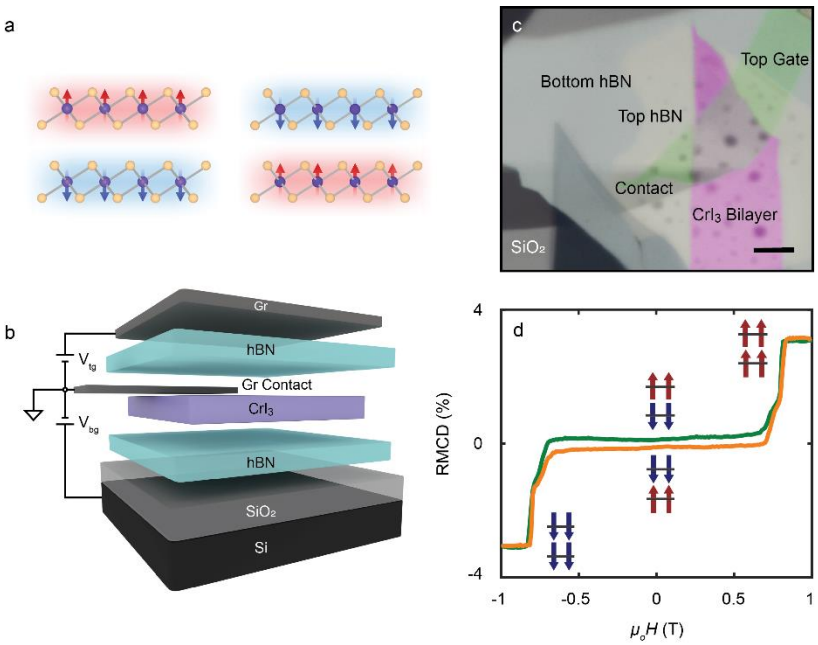

Figure 3.1. **Bilayer gated devices. a)** Magnetic ordering in bilayer CrI_3 in the two energetically degenerate antiferromagnetic ground states, labeled ↑↓ (left) and ↓↑ (right). Cr^{3+} and I^- ions are represented with purple and orange balls, respectively. **(b)** Schematic of a dual-gated bilayer CrI_3 device fabricated by van der Waals assembly. **(c)** False-color optical micrograph of a representative device (Device 1). The scale bar is 5 μm. **(d)** RMCD signal of a bilayer CrI_3 device (Device 1) as a function of perpendicular magnetic field at zero gate voltage.

Figure 3.1d shows a representative RMCD signal of a dual-gated bilayer CrI_3 device (here called Device 1) shown in 3.1c as a function of an out-of-plane magnetic field (μ_oH) at zero gate voltage. The orange curve corresponds to sweeping μ_oH from a negative to a positive value and the green curve shows the time-reversed process. For magnetic fields smaller than 0.8 T, the RMCD signal nearly vanishes, corresponding to the layered AFM states observed in bilayer flakes

(chapter 2 section 4), either ↑↓ or ↓↑ shown in figure 3.1a. However, unlike the as-exfoliated bilayer samples measured without vdW assembly, there is a small remnant RMCD signal, implying that the net magnetization is not completely suppressed in the AFM configurations. This remnant RMCD signal is often observed in bilayer devices that have been through multiple fabrication steps in the vdW assembly process. This could be caused by breaking out-of-plane symmetry of the bilayer during device fabrication, such that the magnetizations from the two layers do not exactly cancel. At a critical field, $\mu_o H_c$ = ±0.8 T, the RMCD signal shows a sudden jump from near-zero up to 3%. This is consistent with as-exfoliated bilayer CrI_3, where that an external magnetic field drives a metamagnetic transition in which the bilayer switches from the layered AFM states (↑↓ or ↓↑) to an FM state (↑↑ or ↓↓).

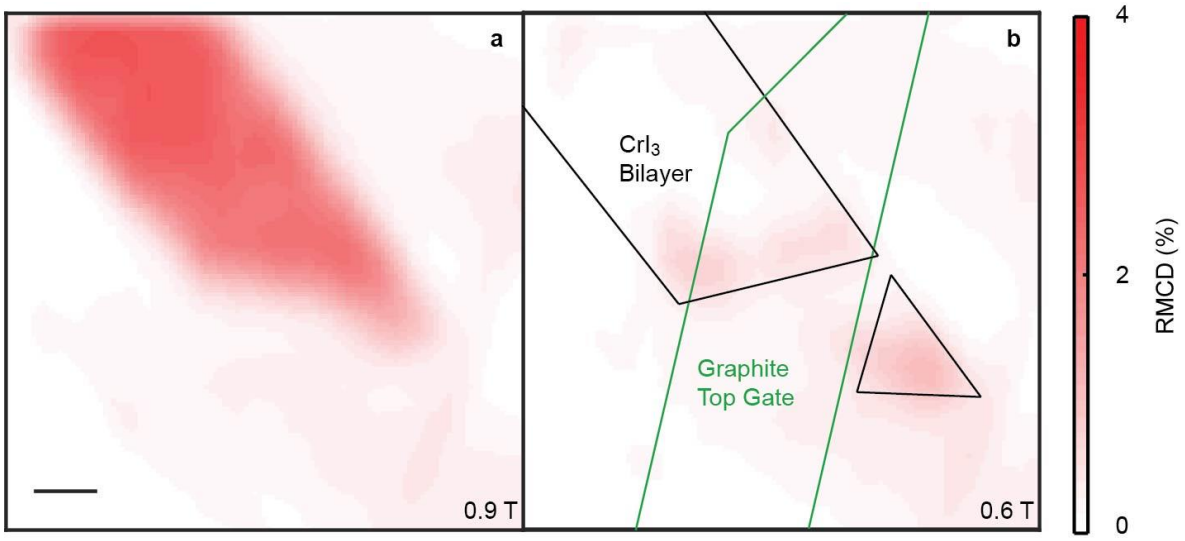

Figure 3.2. RMCD maps at fixed magnetic fields**.** RMCD map of Device 1 in the absence of gate voltage with an applied magnetic field values of **(a)** 0.9 T and **(b)** 0.6 T.

Figure 3.2 shows spatial maps of the RMCD signal over the bilayer flake at 0.9T (a) and 0.6T (b). At 0.9T, which is above the critical field, the bilayer is in the spin-aligned state oriented spin up and RMCD signal is uniform over the entire bilayer flake. When the applied field is 0.6T, which is below the critical field of the bilayer, the entire flake shows little to no RMCD signal. The homogeneity of the signal across the entire flake indicates that the bilayer magnetic behavior is robust against multiple sample fabrication steps and lithographic patterning of electrodes, and the integrity of the flake has not been destroyed.

3.4 Gate Dependence of Metamagnetic Transition

Upon application of a gate voltage, The metamagnetic transition is highly controllable by electrostatic gating. MOKE measurements were taken on a second type of device (here called Device 2) fabricated with only a silicon gate, while varying both the magnetic field and gate voltage.

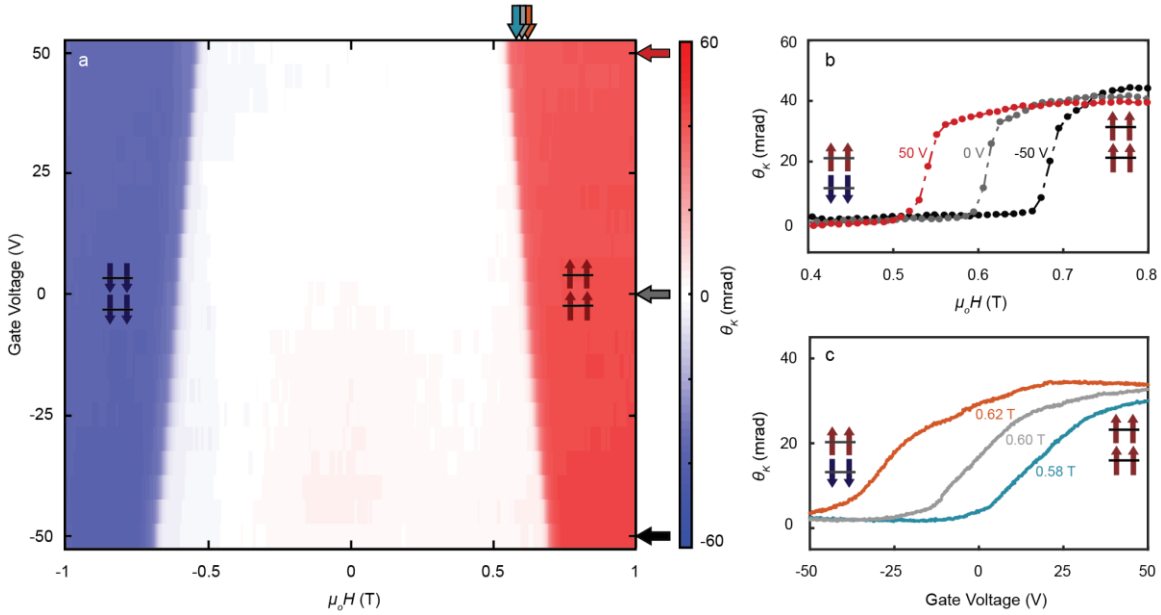

Figure 3.3. **MOKE signal vs. gate voltage and applied magnetic field[48]. (a)** Intensity of the polar MOKE signal of a non-encapsulated bilayer CrI_3 device

(Device 2) as a function of both gate voltage and applied magnetic field. **(b)** Selected horizontal line cuts of (a) demonstrating the gated induced change in critical field of the metamagnetic transition at V_{bg} = -50 V (black), 0 V (gray), and 50 V (red). **(c)** Gate induced transition from layered antiferromagnetic to ferromagnetic states at selected $\mu_0 H$ = 0.58 T (blue), 0.60 T (gray), and 0.62 T (orange).

In this device, the bilayer CrI_3 is uncovered and has not been subjected to multiple fabrication steps. Figure 3.3a shows a plot of MOKE intensity as a function of the back gate voltage (V_{bg}) and $\mu_o H$ (sweeping the field down from 1 to -1 T). In this magnetic phase diagram, the white central region represents low MOKE signal arising from a layered AFM state, while the darker red and blue colors represent the two FM states with strong MOKE signals of opposite signs. Based on this phase diagram, the phase boundary, *i.e.* the critical field for the metamagnetic transition, strongly depends on V_{bg}[48].

Figure 3.3b compares the magnetic field dependence at V_{bg} = 0 V and ±50 V by taking horizontal line cuts of the phase map shown in Figure 3.3a. The critical field $\mu_o H_c$ has shifted by roughly 0.2 T, from 0.7 T at -50 V to 0.5 T at 50 V. This shift in $\mu_o H_c$ is bidirectional and linear - when a positive gate voltage is applied, the absolute value of the critical field is decreased, and vice versa for negative gate voltages.

In addition to altering the critical field of the bilayer and observing this as a function of $\mu_o H$, as a result of the large modulation in $\mu_o H_c$ it is also possible to realize a switch from the AFM to FM by sweeping the gate for fields fixed near the MM transition. Figure 3.3c illustrates this electrically controlled magnetic phase transition at three selected magnetic fields, corresponding

to vertical line cuts on the phase map in Fig. 3.3a. The MOKE signal starts near zero at negative gate voltages, corresponding to AFM ordering. As the voltage increases to a critical value, the MOKE signal quickly rises and reaches a saturated value, demonstrating electrical switching to the FM state. For the three selected magnetic fields ranging from 0.58 T to 0.62 T, the required voltage to initiate the transition from the layered AFM states to the FM ↑↑ state shifts towards positive gate voltage with decreasing applied magnetic field.

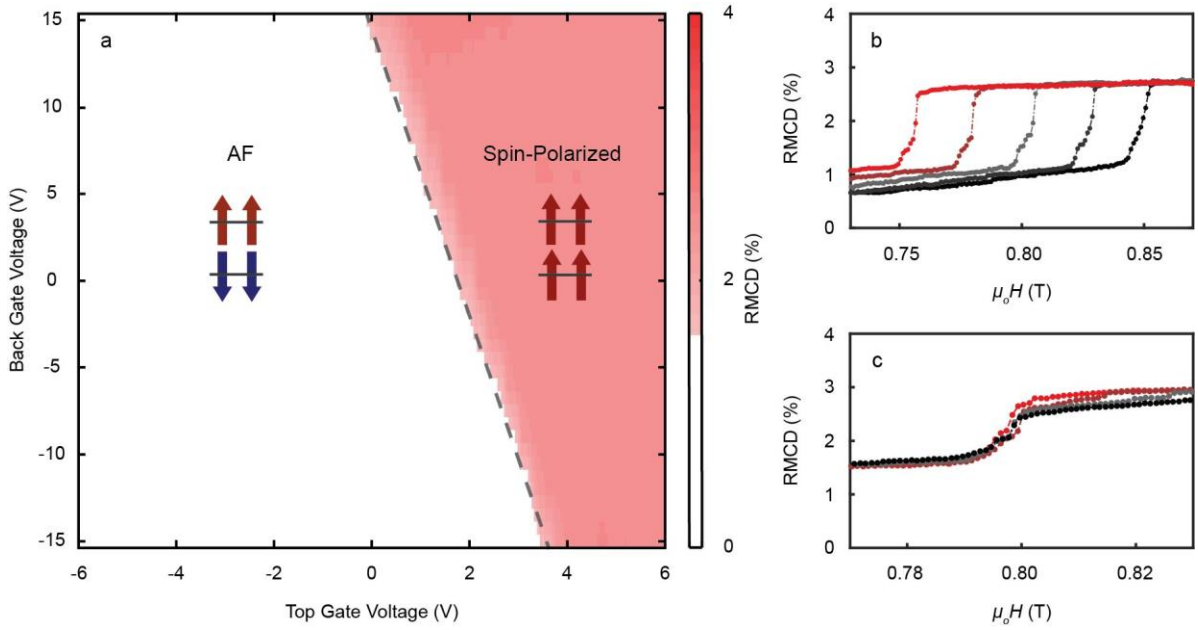

Figure 3.4. **Origin of voltage-controlled metamagnetism. (a)** RMCD signal of a dual-gated device (Device 1) when sweeping both the graphite top gate and silicon back gate. (**b**) RMCD signal of the same device as a function of applied magnetic field at fixed doping levels from 0 cm^{-2} (black) to 4.4×10^{12} cm^{-2} (red) for zero displacement field. **(c)** RMCD signal as a function of applied magnetic field at several displacement fields ranging from 0 V/nm (red) to 0.6 V/nm (black) for zero doping.

In single-gated devices, an applied gate voltage introduces both an interlayer bias and layer-dependent electrostatic doping. To determine which of the two effects dominates the gate-tunable magnetic phase transition, we fabricated a dual-gated device to enable independent control over the doping and electric field. After identifying the critical field for the metamagnetic transition, we fixed the magnetic field near the transition and measured the RMCD signal as a function of both gates.

Figure 3.4a shows the RMCD intensity plot as a function of both top and back gate voltages at $\mu_o H$ = 0.78 T. The graphite top gate was swept between ±6 V and the silicon back gate between ±15 V. The red region on the right is the large, positive signal from the ↑↑ state while the white region on the left is the much smaller signal from the layered AFM state. Using a parallel-plate capacitor model (See section 3.5), it is possible to calculate the constant-doping and constant-field contours on the phase map. In this device, the constant doping line lies parallel to $V_{TG} = -\frac{3}{34}V_{BG}$, while the constant field line lies parallel to $V_{TG} = +\frac{3}{34}V_{BG}$. The metamagnetic transition, *i.e.* the boundary between the red and white regions, lies nearly parallel to the constant-doping contours as indicated by the dashed line in Fig. 3.4a. To further confirm this, we carried out magnetic field sweeps of the RMCD signal at several doping levels with the same displacement field (Fig. 3.4b), and at several displacement fields with the same doping level (Fig. 3.4c). These clearly show that the doping level dominantly affects the critical field, since there is little to no change in the metamagnetic transition when the displacement field is varied (Fig. 3.4c). This is not surprising since in other magnetic systems, doping leads to modulation of orbital occupation and magnetic anisotropy, and thus a change in the magnetism. The physical reason for the modulation of the critical field as a function of doping in this specific system however is still unknown.

3.5 Parallel Plate Capacitor Model

Following the methodology from Zhang *et al.* and Taychatanapat *et al.*[49,50], the dual-gated bilayer CrI_3 devices can be approximated as a parallel-plate capacitor to obtain the constant doping (*n*) and constant electric displacement field (**D**) contours for the dual gate phase map. Here, the top and bottom graphite gates function as the two plates of the capacitor. The amount of doping, *n*, in the device is then:

$$n = C_{BG}(V_{BG} - V_{BG}^{D}) + C_{TG}(V_{TG} - V_{TG}^{D})$$

where *C* is the areal capacitance, V_{BG} and V_{TG} are the back gate and top gate voltages, respectively, and V_{BG}^{D} and V_{TG}^{D} the charge neutral point voltages. Since the aim of this calculation is to show whether the metamagnetic transition shown in Fig. 3a arises from a change in *n* or a change in **D**, we can find a constant-doping contour by setting $n = V_{TG} = V_{BG} = 0$, as these terms only offset the contour by an arbitrary constant. The areal capacitance is given as: $C = \varepsilon/d$, where ε is the permittivity of the dielectric layer and *d* is the thickness of the dielectric layer (in our case, the hBN flakes used as the dielectric layers). Including the bottom hBN encapsulation layer with the SiO_2 dielectric layer in the bottom areal capacitance, equation (1) for Device 1 simplifies to:

$$V_{TG} = -\frac{d_{hBN}}{\frac{\varepsilon_{hBN}}{\varepsilon_{SiO_2}} d_{SiO_2} + d_{hBN}} V_{BG}$$

The out-of-plane static dielectric constants of hBN and SiO_2, ε_{hBN} and ε_{SiO2} respectively, are 4 and 3.9[51]. The device sits on top of 285 nm SiO_2 substrate, and both top and bottom hBN flakes were approximately 30 nm. Similarly, we can also obtain the zero-displacement field contour by starting with the general expression for the applied displacement field:

$$\boldsymbol{D} = C_{BG}(V_{BG} - V_{BG}^{D}) - C_{TG}(V_{TG} - V_{TG}^{D})$$

and removing the same terms:

$$V_{TG} = +\frac{d_{hBN}}{\frac{\varepsilon_{hBN}}{\varepsilon_{SiO_2}} d_{SiO_2} + d_{hBN}} V_{BG}$$

For the device used in this study, we obtained $V_{TG} = -\frac{3}{34} V_{BG}$ for the constant doping line, and $V_{TG} = +\frac{3}{34} V_{BG}$ for the constant displacement line.

3.6 Gate Control of AFM States

In addition to gate-voltage tuning of the metamagnetic transition, it is possible to further realize electrical control of the layered AFM states at zero magnetic field. We first prepare the system by starting in the ↑↑ state with an applied magnetic field of 1 T, and then sweeping the field back to zero (Initialization 1, inset Fig. 3.5a). Remaining at zero external magnetic field, we sweep the back gate voltage and observe a MOKE signal linearly dependent on the voltage with a slope of -0.04 mrad/V, shown in Fig. 3.5a. Similarly, we prepare the bilayer to its time-reversal state by starting in the ↓↓ state with a magnetic field of -1 T and sweeping the field back to zero (Initialization 2, inset Fig. 3.5b). In Fig. 3.5b, the MOKE signal also exhibits a linear dependence on the gate voltage, but with an opposite slope of 0.04 mrad/V. These results demonstrate that the two initialization processes lead to two distinct layered AFM states, ↑↓ and ↓↑, which are time-reversed pairs, and that the AFM states can be tuned electrically even at zero magnetic field.

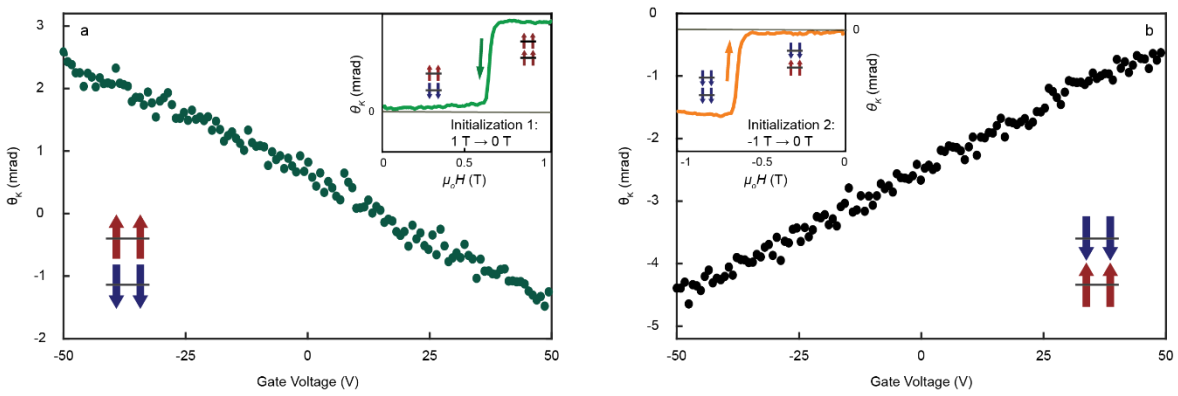

Figure 3.5. **Gate-voltage induced MOKE of layered AFM states**[48]. **(a)** Gate-dependent MOKE signal of a bilayer CrI_3 device (Device 2) prepared in the ↑↓ state following the initialization depicted in the inset. **(b)** Equivalent measurement performed on the device prepared in the ↓↑ state by the initialization process in the inset.

This observed magnetoelectric coupling in the layered AFM states can be explained by the spin-layer locking effect. For an AFM state at zero field, the spin (magnetization) orientation is locked to the layer pseudospin that labels the geometric top and bottom layers (figure 3.1a). A direct consequence of this spin-layer locking effect is that the creation of a layer polarization is accompanied by a net magnetization. In the AFM configuration, the opposite spin orientations of the two layers quench the interlayer hopping and hence the layer hybridization. The application of an electrostatic gate voltage then creates a layer polarization of the carriers, resulting in net magnetizations of opposite signs in the ↑↓ and ↓↑ states. The layer polarization and hence net magnetization has a linear dependence on the gate voltage, consistent with the observed gate dependence of the MOKE signal in Fig. 3.5.

This also allows us to identify and controllably access the two energetically degenerate AFM states. The application of a positive gate voltage results in a larger electron density in the bottom

layer than in the top layer. If the bilayer is in the ↑↓ state, the net magnetization then points down with a negative slope of the MOKE signal as a function of gate voltage. The ↓↑ state will then have a positive slope in the gate-dependent MOKE signal. Although the device assembly process may already break the degeneracy between the ↑↓ and ↓↑ states, the signs of the gate-dependent MOKE slopes are nevertheless fingerprints for distinguishing between the two AFM states. Based on Figs. 3.5a and b, it is possible to determine that using Initialization 1, the ↑↑ state transitions to the ↑↓ state, and by using Initialization 2, the ↓↓ state transitions to the ↓↑ state.

3.7 Final Remarks

These results demonstrate two forms of electrical control of magnetism in bilayer CrI_3. First, in an applied magnetic field, the critical field for the metamagnetic transition can be tuned several hundreds of mT, allowing a gate voltage driven phase transition from a layered AFM phase to an FM phase. Dual gate studies show that the mechanism is dominated by electrostatic doping. Second, at zero magnetic field, the net magnetization can be continuously tuned by gate voltage. The two antiferromagnetic states, ↑↓ and ↓↑, show the same linear dependence of the MOKE signal on gate voltage but with opposite signs, which provides an experimental measure to distinguish these two degenerate magnetic states. Similar work on bilayers and monolayers of CrI_3 has shown an even large tunability of the metamagnetic transition[52]. This study demonstrated that the critical field can be tuned continuously to 0T for electron doping above about $2.5 \times 10^{13}/cm^2$, causing an FM-AFM transition in the absence of an applied field[52]. The studies on electrical control of magnetism in CrI_3 show that van der Waals magnets provide a new system for exploring magnetoelectric effects, with large potential for external control of their magnetic properties.

Chapter 4. MONOLAYER WSE_2 – SCALABLE GROWTH AND SINGLE QUANTUM EMITTERS

While transition metal dichalcogenide compounds (MX_2) have been investigated for decades, early studies of band structure and optoelectronic properties focused on bulk crystals, as well as crystals suspended in solution or cleaved to several hundred nanometers[53,54]. Following the successful isolation of graphene and discovery of new physics arising in the mono and several layer limit[19,55], attention once again returned to the layered transition metal compounds. With mechanical exfoliation techniques to isolate single and few layer samples, they have again become a focus of intense research. Like graphene, they show a range of new physics and potential applications in the few layer limit, making them promising materials for nanoscale devices and developing quantum technologies. In this chapter, I summarize the optical selection rules and valley physics of excitons in monolayer MX_2 materials. I then describe the scalable growth of monolayer WSe_2 flakes and characterization of their intrinsic exciton behavior, as well as the discovery of a new type of single photon emitters in the CVD grown WSe_2 monolayers.

4.1 Crystal Structure and Valley Physics

MX_2 materials are composed of a central layer of transition metal atoms (M) coordinated to layers of chalcogen atoms (X) above and below in an X-M X sandwich structure[17,18,56,57]. Coordination of the metal atom and unit cell geometry both vary as a function of metal d-electron count[56], but all compounds show strong covalent in-plane bonding. This separates the material into individual X-M-X layers, leaving only weak inter-layer interactions due to Van der Waals forces.

Variation of the metal and chalcogen components yields a wide variety of material properties, ranging from insulators like Hf_2 to metals like $NbSe_2$, while some compounds like $NbSe_2$ and $TaSe_2$ show more exotic behavior such as superconductivity and charge density waves.

The most commonly studied are group VIB semiconducting compounds (MoS_2, WS_2, WSe_2, $MoSe_2$).

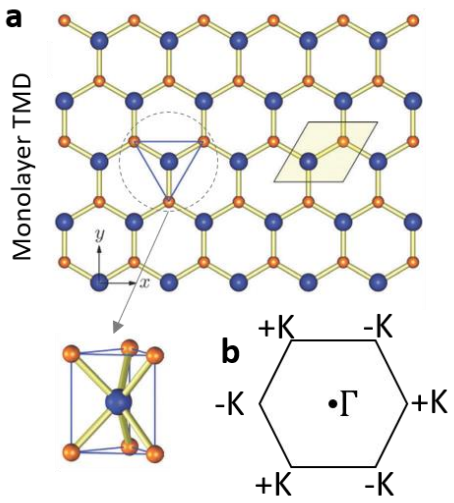

Figure 4.1. **Monolayer TMD Crystal Structure. a)** Monolayer MX_2 lattice for trigonal prismatic coordination. Orange corresponds to chalcogen atoms, blue to metal atoms. Dotted outline: Monolayer trigonal prismatic unit cell. **b)** Hexagonal 1st Brillouin zone.

They show trigonal prismatic coordination of the central metal atom, with a trigonal prismatic monolayer unit cell (Fig. 4.1a, dotted outline) and hexagonal first brillouin zone (BZ) (Fig. 4.1b)[58–60]. The predominant polytype is the 2H hexagonal phase characterized by an A-B-A stacking geometry which leads to a D^4_{6h} crystal space group for any even layer-number flakes[59,60].

Monolayers, tri-layers and other odd layer numbers show symmetry breaking (loss of inversion symmetry) and are characterized by the D_{3h} point group. The strong spatial confinement within each layer combined with the symmetry breaking in the monolayer limit lead to a unique band structure and a broad range of novel physics emergent in the mono and few-layer limit.

Metal-chalcogen covalent bonds are composed primarily of chalcogen s and p orbitals, while the metal d orbitals remain non-bonding[59]. Based on the coordination geometry of the central metal atom, the d orbitals hybridize and their degeneracy is lifted. In compounds with trigonal prismatic coordination, the metal d orbitals split into three groups according to their irreducible representations in the D_{3h} point group, d_{z^2} (a1), $d_{x^2-y^2}$ and d_{xy} (e), and d_{xz} and d_{yz} ($e^{'}$). The a1 and e groups show a large ~1 eV splitting that forms the monolayer direct bandgap[59].

The band structure is highly dependent on layer number. As layer number decreases, the indirect bandgap at the Γ points widens due to sensitivity of the constituent orbitals to layer separation. The direct gap at the K and –K points is composed mainly of non-bonding d orbitals localized at the central metal atoms, and it shows little sensitivity to layer number. As a result, monolayers show a transition to a direct bandgap at the K points, and the magnitude of the gap is determined by the hybridization and splitting of the non-bonding metal d orbitals[17,18].

The monolayer band gap at the K points results primarily from d_{z^2} orbitals (conduction band) and $d_{x^2-y^2}$ and d_{xy} orbitals (valence band)[59]. Due to broken inversion symmetry in monolayers, the K and –K points are inequivalent even though they are energetically degenerate, and are related by a time reversal operation. As a result, monolayer samples are expected to show valley contrasting circular dichroism in their optical transitions, providing a convenient means of addressing the specific valley index of band edge excitons[58,60]. Due to the large orbital angular momentum of the orbitals that comprise the valence band at the K valleys, large spin orbit coupling splits the valence

band by several hundred meV. This spin splitting is reversed in the K and –K valleys as a result of the time-reversal operation relating the valleys, leading to a unique coupling between the spin and valley degrees of freedom of band edge excitons[60].

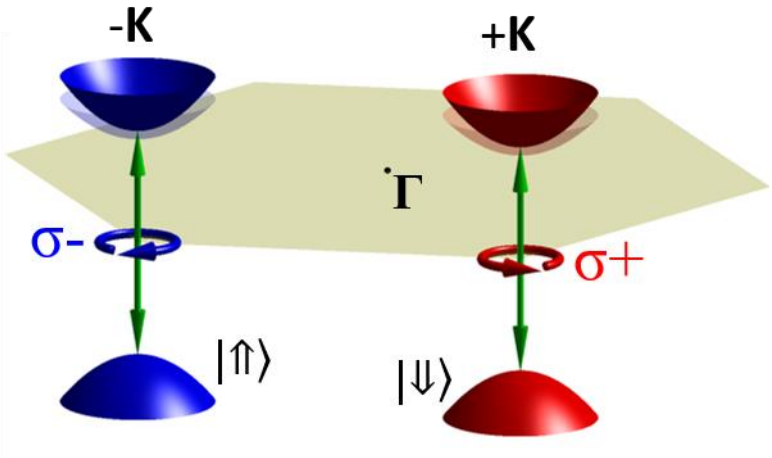

Figure 4.2. **TMD valley structure**. Band structure at the K and –K valleys, including spin orbit splitting, shows both valley and spin-orbit effects as well as helicity dependent optical selection rules for the two valleys.

Figure 4.2 summarizes the monolayer band structure at the K and –K valleys for prototypical group VI-B TMD's[58]. Band edge excitons can reside in either of the energetically degenerate but inequivalent K valleys, giving them a binary valley degree of freedom. Large spin orbit coupling at the K and –K points splits the valence band (top band shown), and lack of inversion symmetry in monolayers links the spin degree of freedom of carriers to their valley index. Due to the direct bandgap, these properties are accessible optically. Valley contrasting circular dichroism, a direct consequence of inversion symmetry breaking, means that it is possible to selectively address each valley via the polarization state of incident photons. Right circularly polarized photons will create excitons in the one valley while left circular excitation will populate the other valley.

Control of both spin and valley degrees of freedom has been investigated in other materials. Earlier quasi-2D semiconducting systems such as AlAs quantum wells have been studied as potential candidates for realizing spin and valley control in band edge excitons[64]. In AlAs quantum wells, conduction band electrons have a binary valley degree of freedom at the X points of the Brillouin zone, suggesting the possibility of valley-based logic and devices. Valley populations have been manipulated and measured using strain to lift the degeneracy between the equivalent valleys, suggesting the viability of using them to encode information[64]. However, the two valleys are not intrinsically distinguishable and so external perturbations are necessary to separate them. Monolayer MX_2's are a unique material with an optically accessible direct bandgap as well as coupled spin and valley degrees of freedom that can be easily distinguished and measured through their interaction with light. Unlike earlier quantum wells, they are a truly two dimensional semiconducting system with a wide variety of emergent physics in the monolayer limit. This has led to significant advances in both fundamental research and application in nanoscale devices.

4.2 Motivation for Scalable Growth of Monolayer MX_2's

Despite the promising combination of atomic thickness and optically accessible valley physics, the majority of successful MX_2 devices rely on mechanically exfoliated samples. Exfoliation involves thinning plate-like bulk crystals to several hundred nanometers on scotch tape, and depositing flakes of various thickness, size, and shape on a substrate (usually silicon dioxide). Monolayers are found by searching the entire chip under an optical microscope and their thickness can be confirmed using optical contrast, AFM, PL, or Raman spectroscopy. This is a time-consuming and non-scalable process that will prevent widespread application of MX_2's in any commercial technology. The need for exfoliated samples even limits the scope of fundamental experiments. Exfoliated monolayer flakes are usually small (<20 um edge length), and device

geometry must be adapted to the particular shape of each individual flake. Since monolayer flakes are sparsely distributed on the substrate, studies are almost always limited to investigation of a single flake at a time.

An additional advantage of direct monolayer synthesis lies in the possibility to investigate lattice anomalies such as long range defects (grain boundaries and dislocations) and edges, as well as a variety of point defects. Beyond enabling a more complete understanding of the material properties of MX_2's, monolayer defects could provide a means of localizing excitons further to specific sites within a monolayer. In other solid-state systems, localized single excitons have provided sources of single photon emission, important for a variety of applications in quantum computing and communication. Indium arsenide (InAs) quantum dots are a well-studied example, where excitons localized to quantum dots emit single photons at a time and have shown promise in heterostructure devices controlling and tuning their emission[65–68]. Naturally occurring point defects such as NV-centers in diamond[69] and anti-site defects in 4H-SiC[70] provide a particularly elegant way to confine single excitons within a solid-state system.

However, monolayer MX_2's offer a promising combination of unique physics and material properties that could have several advantages over other systems. If confined excitons inherit the valley physics of the intrinsic 2D excitons, they could provide a way to combine the valley degree of freedom with single photon emission, a desirable combination for quantum computing devices. Unlike other bulk defect matrices, monolayers are atomically thin. Not only could localized excitons in WSe_2 be readily integrated into nanoscale devices, any defects are inherently at the surface of the monolayer. They could potentially be tuned via external perturbations or even deterministically created within a monolayer, an extremely appealing possibility. A significant drawback in current solid state systems is that specific defects tend to form in random spatial

locations. InAs quantum dots form by self-assembly within gallium arsenide heterostructures, and NV-centers and 4H-SiC anti-site defects form randomly in the bulk material. Any investigation of new defects in monolayer semiconductors will likely benefit from a large number of available samples, to unambiguously establish optical properties and structure as well as quantify uniformity and feasibility for future experiments. This could be difficult to attain in exfoliated samples.

A key advantage of exfoliated samples however, has been their high optical quality. Spectrally narrow, well resolved exciton and trion emission peaks are crucial for achieving devices based on the valley and spin of excitons, as well as for any studies exploring valley polarization. Valley and spin-based phenomenon such as polarization and coherence seem particularly dependent on sample quality. Defects and impurities can facilitate exciton inhomogeneous broadening and seem to destroy valley polarization and coherence, possibly via inter-valley scattering. To truly provide a feasible alternative to exfoliated samples, monolayer MX_2 synthesis must not only be cost-efficient and scalable, it also must consistently yield monolayers with comparable optical quality to exfoliated samples.

In parallel with fundamental studies of MX_2's, various synthetic methods have been investigated for scalable monolayer growth. Chemical exfoliation via Li intercalation followed by ultrasonication and purification is a scalable approach that yields monolayer flakes which can be deposited in a film on various substrates[71]. Individual flake sizes are usually several hundred nanometers edge length however, and preparation of a uniform monolayer film using this technique is difficult. Recently, high quality single-crystal samples of MX_2's have been grown using MBE on a variety of substrates with layer-by-layer growth[72]. While this degree of control during synthesis is ideal for achieving the highest quality single-crystal samples and in-situ tunability during growth, it requires access to costly equipment and ultra-high vacuum.

Monolayer growth using chemical vapor deposition (CVD) has shown particular potential, offering a simple means of scalably growing arbitrary MX_2 compounds and heterostructures in large volume[73–75]. The vast majority of studies report successful growth of MoS_2, with large (100um) crystals showing triangular morphology consistent with the monolayer trigonal unit cell. Room temperature optical studies show bright PL similar to exfoliated MoS_2, however few studies report detailed characterization of neutral and charged excitons[73]. Other MX_2 compounds have also been successfully grown using CVD, including lateral heterostructures combining two different MX_2's in a single monolayer[76,77]. CVD synthesis is therefore flexible enough to allow growth of both pure MX_2 compounds and tunability of composition during growth, in addition to large scale synthesis of single crystals. Most growth studies are focused towards eventual commercialization of MX_2 devices however, and lack the rigorous low temperature optical characterization crucial for investigations of fundamental physics.

4.3 CVD Growth Method

The growth procedure is based on simple vapor deposition. Like other reported CVD MX_2 syntheses, growth is carried out in a horizontal tube furnace and uses a carrier gas to transport sublimated precursor materials to the substrate, where they nucleate and grow into crystals. Reproducible high yield growth of monolayers depends sensitively on substrate and source placement within the furnace, as well as gas flow rate and temperature. The parameters have been optimized to favor growth of monolayers, however multilayer and bulk crystals are also obtained.

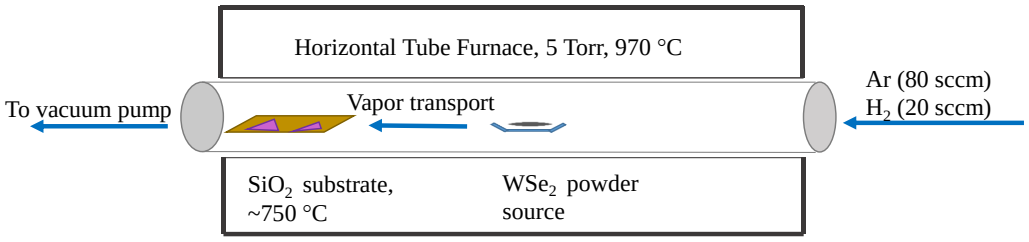

Figure 4.3. **Cartoon of the furnace setup used for CVD synthesis of WSe_2 monolayers.**

Figure 4.3 shows the setup used for growth. Powdered WSe_2 source (about 0.3 g, 99.99% purity Alfa Aesar) in a ceramic crucible is loaded into a 1" diameter quartz tube furnace. The source is placed in the hot zone of the furnace 3-5 cm from the downstream furnace wall. An insulating substrate (about 1x2 inches) typically SiO_2 is placed on the downstream furnace wall, about 1 cm from the edge. The upstream end of the tube is connected to argon and hydrogen carrier gasses (99.98% purity, Praxair), while the downstream end is connected to a mechanical pump.

Before growth, the tube is evacuated to a pressure of < 100mTorr, and purged repeatedly with argon gas. The furnace is then heated to a peak temperature of 970 °C at a rate of about 25 °C per minute, and is held at 970 °C for a 5 to 10 minute growth period. During the growth, argon (80 sccm) and hydrogen (20 sccm) carrier gasses transport sublimated WSe_2 source to the SiO_2 substrate, which is at a much cooler temperature (750 to 850 °C). WSe_2 then nucleates on the substrate and forms crystals. Using this method, triangular single crystal monolayers up to 30 µm in edge length can be grown on SiO_2 substrates, however more typical sizes range from 5 to 15 µm depending on location on the substrate.

4.4 PHOTOLUMINESCENCE STUDIES OF CVD MONOLAYERS

The resulting WSe_2 crystals are initially characterized using optical microscopy and atomic force microscopy (AFM). Figure 4.4a shows an optical image of the SiO_2 substrate after a typical growth where a variety of growth morphologies are present at different locations on the substrate. Figure 4.4b shows crystals that form at the end of the substrate closest to the hot zone of the furnace (region "i" in figure 4.4a). They are isolated, equilateral triangles with edge dimensions of ~ 30 μm. The triangular shape suggests a lack of grain boundaries or other long-range defects. Thicker triangular crystals are distinguishable from monolayers by optical contrast, with darker colors corresponding to bi- and tri- layer crystals.

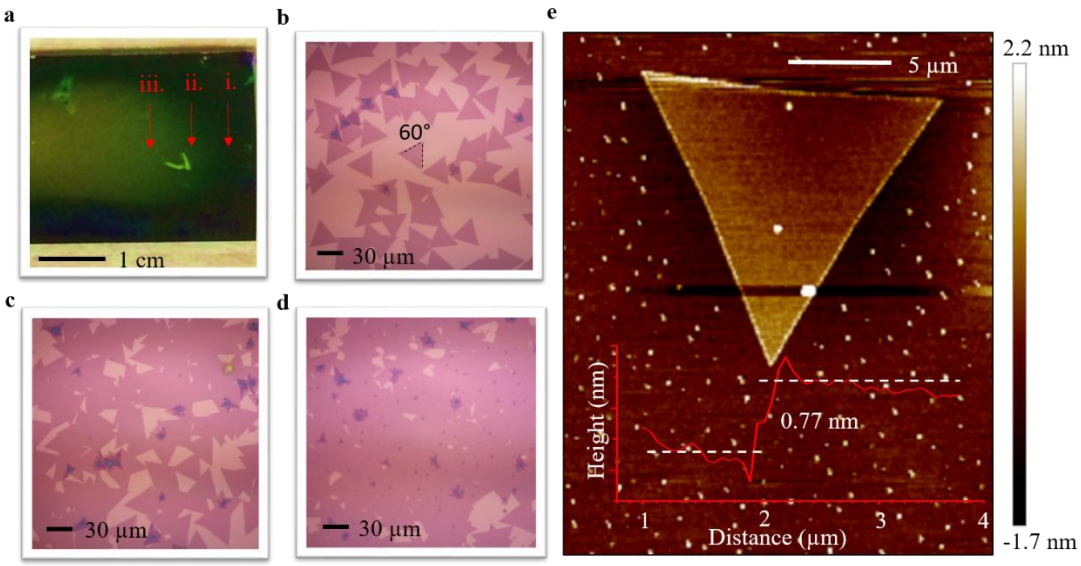

Figure 4.4. **Optical Characterization of CVD Monolayers. a)** Optical image of a typical SiO_2 substrate after growth, showing three different regions corresponding to regions with different growth morphologies. **b)** Growth from region "i" in a), showing triangular crystals with edge length ~ 30μm. **c)** Growth from region "ii" showing denser coverage. **d)** Growth from region "iii", showing predominantly a

continuous monolayer film. **e)** AFM image of a monolayer triangular crystal, with a plot showing edge height for a line cut.

Growth from the middle location on the substrate, slightly further from the hot zone of the furnace (region "ii" in Fig 4.4a) shows much denser monolayer coverage, suggesting a significantly higher nucleation density likely due to the lower temperature. At even further locations on the substrate (region "iii"), the growth becomes a single monolayer film interspersed with smaller bilayer regions (Fig 4.4d). Figure 4.4e shows an atomic force microscope image of a triangular flake, revealing that the surface is uniform and flat. A line cut across one edge of the triangle shows an apparent thickness of ~0.75 nm, the same as for exfoliated monolayers on SiO_2 substrates.

Room temperature PL is not generally a sensitive test of sample quality in these materials, and also cannot probe the optical selection rules for valley excitons. To rigorously characterize the optical quality of the CVD monolayers compared to exfoliated WSe_2, low temperature PL is used. Monolayer samples on SiO_2 are placed in a helium-flow cryostat and cooled a temperature of 30K or lower for low temperature measurements. CW excitation is reflected off a dichroic beam splitter through a 40X objective, and onto the sample through the transparent window of the cryostat. PL is collected through the same objective and passes through the dichroic beam splitter and a laser notch filter. The spectrum is measured using a Princeton Instruments Acton 2500i grating spectrometer and an Andor Newton CCD (charge-coupled device).

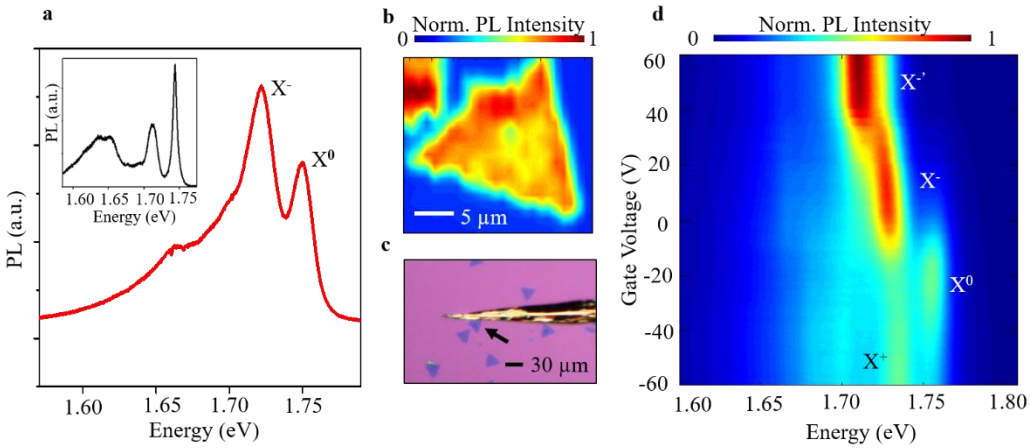

Figure 4.5. **PL Characterization of CVD WSe_2. a)** PL spectrum for CVD monolayer at 30K, showing emission from neutral and charged excitons X^0 and X^-. Inset: PL spectrum for an exfoliated sample at 30K. **b)** Spatial map of PL from CVD monolayer. **c)** Optical microscope image of CVD growth monolayers on an SiO_2 chip with an indium contact to allow electrostatic gating. **d)** PL as a function of gate voltage showing charge tunable emission from X^0, as well as both X^- and X^+.

Figure 4.5a shows a typical PL spectrum for CVD-grown monolayers, taken at 30 K using a 532 nm excitation laser. Well resolved features are present at 1.722 and 1.749 eV due to emission from neutral and charged excitons, in good agreement with the typical values for an exfoliated monolayer (inset). A spatial map of the integrated PL spectrum over a single monolayer flake (Fig 4.5b) shows a uniform PL intensity over the entire flake indicating homogeneous sample quality.

In order to compare the electrostatic tuning of exciton species in CVD samples with results established for exfoliated WSe_2, a simple electrical contact can be made using either indium melted directly on the monolayer or gold evaporated onto a lithographically defined pattern. Figure 4.5 c shows an optical microscope image of CVD WSe_2 flakes on an SiO_2 chip with an indium contact

touching one of the flakes. The sample can then be electrostatically doped with holes or electrons by tuning the voltage on the doped silicon substrate, while monitoring changes in the PL spectrum similar to studies on exfoliated samples. Figure 4.5d is a plot of PL intensity versus energy and substrate gate voltage V_g. This sample shows slight intrinsic negative doping, since the neutral exciton is most prominent at negative gate voltage. Near V_g = -25 V it is approximately neutral and the observed PL at 1.749 eV is dominated by the neutral exciton (X^0). For V_g < -25 V hole doping leads to formation of the positively charged exciton X^+. Similarly, for V_g > -25 V electron doping promotes formation of the negatively charged trion X^- at 1.722 eV. For V_g > 20 V, the lower energy feature ($X^{-\prime}$) appears and persists up to 60 V consistent with reports on exfoliated samples[78,79]. The clearly resolvable exciton and trion features show that the neutral and charged excitons in the grown monolayers are completely electrostatically tunable, demonstrating that the grown monolayers are suitable for device applications previously only explored with exfoliated samples.

To establish the viability of the monolayers for investigating valley-based phenomenon and valleytronic applications, polarization-resolved PL is used to measure the degree of valley polarization and coherence. Similar to studies on exfoliated MoS_2 and WSe_2 samples, light with a specific helicity (σ^+ or σ^-) is used as excitation, and the PL is measured for both co-polarized emission and cross polarized emission. Figure 4.6a shows the PL with σ^+ and σ^- detection, for excitation with σ^+ polarized light at a temperature of 30 K. Co-polarized emission (red curve) is significantly stronger than cross polarized emission (blue curve), indicating that emission from both the neutral and charged excitons shows substantial valley polarization (~30%), comparable to results obtained for exfoliated samples.

In addition, it is also possible to generate and observe valley coherence between +K and –K states using linear polarization resolved PL measurements. The degree of observed valley coherence in WSe_2 samples seems particularly dependent on sample quality, and so provides a good comparison to determine the feasibility of using the CVD WSe_2 samples for experiments depending sensitively on the valley index of excitons. In samples with minimal valley decoherence, excitonic quantum coherence is maintained longer than the exciton relaxation time. Inter-valley coherence can then be determined from the degree of linear polarization of the neutral exciton PL.

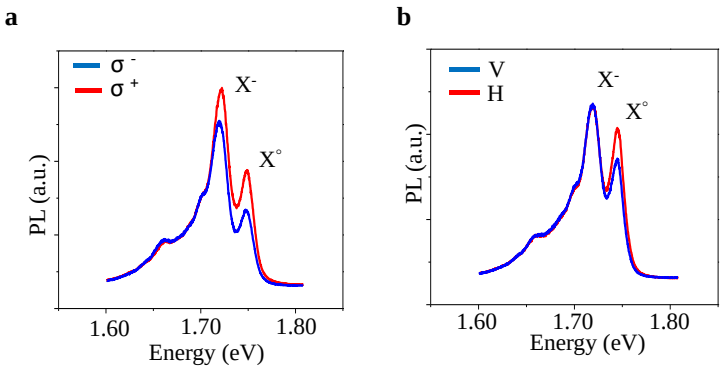

Figure 4.6. **Polarization resolved PL. a)** Valley polarization observed in CVD WSe_2 monolayers. Red curve corresponds to σ^+ detection, blue curve corresponds to σ^- detection, for σ^+ excitation. **b)** Valley coherence observed in CVD WSe_2. Red curve corresponds to horizontal detection, blue to vertical detection, for horizontal excitation.

Figure 4.6b shows the PL spectra obtained for vertical (blue) and horizontal (red) detection with horizontally polarized excitation. Linearly polarized emission is observed for neutral excitons but not for trions, in agreement with previous reports of valley coherence in monolayer WSe_2.

4.5 Defect-Bound Excitons in CVD WSe_2

In the process of measuring low temperature PL of the synthesized monolayers, we have observed bright and narrow emission lines in many samples when they are cooled to temperatures near 5K[80]. I have since observed similar narrow emission in almost all WSe_2 monolayers grown using this method, and it has also been seen by other research groups in exfoliated WSe_2 samples[81–84].

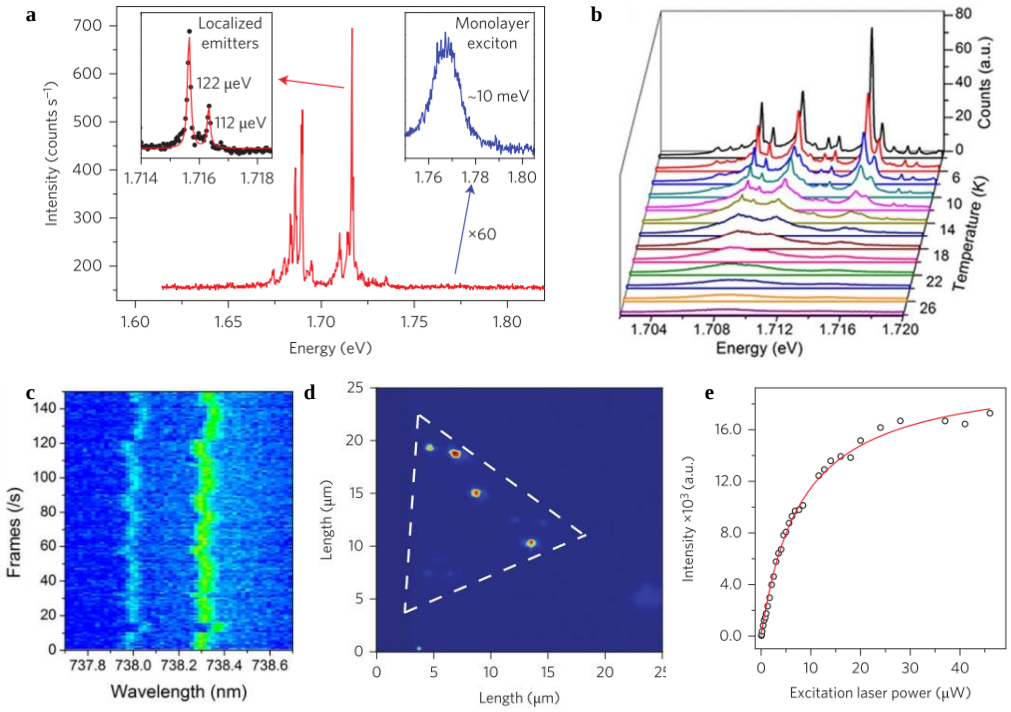

Figure 4.7. **Optical characterization of emitters. a)** Narrow emission peaks from monolayer WSe_2 at 5K. Inset 1: Emission from intrinsic exciton, significantly weaker than narrow peaks. Inset 2: Doublet fine structure of a single emitter. **b)** Temperature dependence of narrow emission lines. **c)** Spectral diffusion for a single doublet. **d)** Spatial map of emission in the range 1.719 +/- .006 eV. **e)** Power dependence of PL emission for narrow emitter.

Figure 4.7a shows a typical PL spectrum from CVD-grown WSe_2 monolayers at 5K. Emission from several narrow peaks within the excitation beam spot is visible, significantly stronger than emission from the intrinsic neutral exciton (located at 1.77 eV). These emission lines consistently occur in the energy range 40 to 100 meV below the neutral exciton (between 720 to 800 nm). The emission lines also show a pronounced temperature dependence (Fig. 4.7b), with weak emission and broad linewidths (several nm) at temperatures above about 20K. Upon cooling the sample further to 4K, the lines narrow to <150 μeV and increase significantly in intensity.

The narrow lines show a doublet fine structure, with two peaks separated by a ~0.7 meV (0.3 nm) splitting (Fig 4.7a, left inset). This doublet structure and splitting is highly consistent between all measured emitters over a large range of different samples and growths. The narrow lines show mild spectral diffusion, or variation in the energy of their emission when monitored over time. This spectral diffusion is likely due to fluctuations in the local environment of the emitters and is often present in spatially confined systems like quantum dots. Synchronous spectral diffusion is observed between the two peaks of each doublet (Fig. 4.7 c), further evidence that this is the fine structure of a single emitter and not emission from two energetically similar emitters.

The narrow emission lines are also highly spatially localized within a monolayer. Figure 4.7d shows a spatial map of integrated PL intensity for the spectral window 1.719 +- .006 eV, where the laser spot was stepped over the sample in 0.3 μm increments acquiring a single spectrum at leach location. Isolated bright spots in the map (red dots) show that the emission is from distinct locations on the monolayer (outlined in white dashed line). This is true of all measured emitters in both CVD and exfoliated samples, and highly suggests that the emission is from excitons that have been additionally confined within the monolayer at impurities or lattice defects. The bright spots

are randomly distributed over monolayers, and their density per monolayer varies between growths but is fairly consistent for monolayers of the same growth.

Unlike the neutral exciton and trion, the narrow lines show a pronounced saturation with increasing power. Figure 4.7e shows the integrated PL intensity of a single emitter as a function of excitation power. While intrinsic excitons show a linear dependence on power, PL from the emitter shows pronounced saturation at excitation power greater than 25 μw. Both the ultra-narrow emission linewidths and saturation behavior are consistent with the picture of a single exciton confined to a point within the monolayer due to a structural defect or other lattice inhomogeneity. As a result of the additional confinement, the exciton can now occupy a series of discreet atom-like energy levels, leading to ultra-narrow emission lines free from ensemble broadening seen in intrinsic exciton emission. Furthermore, saturation behavior at large excitation power is typical of two-level atom-like systems, where the excited electron must relax before the system can absorb a photon and become re-excited. It is therefore limited by the lifetime of the emitter.

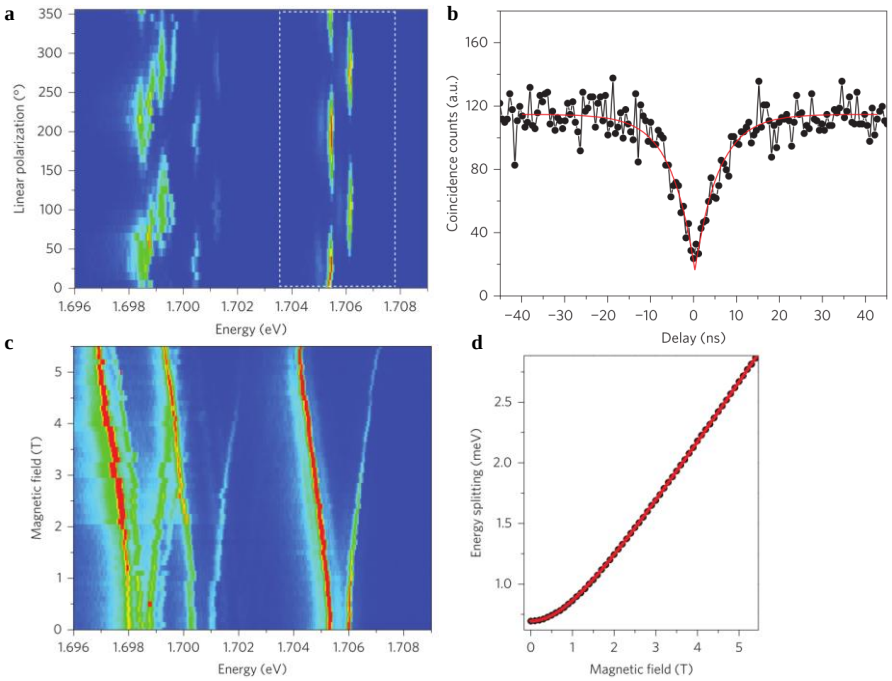

Figure 4.8. **Polarization and Magneto-PL**[80]. **a)** PL intensity for several doublets within the excitation beam spot, as a function of energy and polarization detection angle. **b)** Second order correlation measurement of the emission from a single doublet. **c)** PL intensity plot for several doublets as a function of applied magnetic field. **d)** Zeeman splitting of the doublet at 1.706 eV as a function of magnetic field. Taken from reference 80.

Polarization-resolved PL studies reveal that the doublet is composed of cross-linearly polarized transitions. Figure 4.8a shows a plot of PL intensity as a function of polarization detection angle, where the lines of the most clearly observable doublet (dotted white outline) show a characteristic dependence on polarization angle 90 degrees separated from each other. The degree of polarization for all measured doublets is close to 100%[80].

Importantly, the confined excitons in WSe_2 emit single photons at a time. Using a Hanbury Brown and Twiss-type interferometer, the second order correlation function of the emission from

a single doublet was measured. Excitation from either a CW 637nm laser or pulsed 532nm emission from a Ti:Saph Mira was focused through an objective onto the sample housed in an AttoDry cryostat. The single photon emission was then collected by the same objective and sent through a 50/50 beam splitter to either of two single photon counting avalanche photodiodes. Coincidence events as a function of delay time τ are recorded to build up a histogram, $g^2(\tau)$. The resulting plots (Fig. 4.8b) show a distinct antibunching dip at τ=0, indicating that at a delay time of zero the probability that both detectors receive a photon goes to zero. The dip is well below the established threshold of 0.5, indicating that the confined excitons emit single photons.

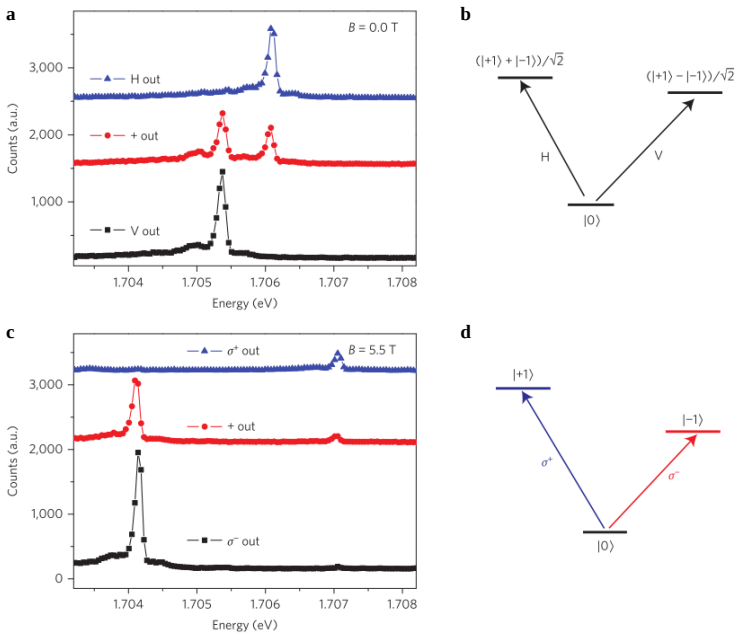

Figure 4.9. **Polarization selection rules. a)** Emission from a cross linearly polarized doublet for horizontal, 45°, and vertical detection. **b)** Linearly polarized selection rules at zero magnetic field. **c)** At large magnetic field (here 5.5 T), the doublet becomes circularly polarized. **d)** Circularly polarized selection rules. Taken from reference 80.

The polarization and splitting of the emitters shows a strong dependence on magnetic field. In a field applied perpendicular to the sample (Faraday geometry), the doublets show large Zeeman splitting as the magnetic field is increased to 5.5 T (Fig. 4.8c). All doublets within the beam spot show similar Zeeman splitting of up to 2.85 meV at 5.5T (Fig. 4.8d), leading to an extracted exciton g-factor of about 8.7, more than twice the value for intrinsic excitons[85,86]. As the Zeeman splitting increases, the doublet switches from being linearly polarized to circularly polarized with one line showing σ^+ emission and another showing σ^- (Fig. 4.9 a,c). The selection rule now resemble the regular WSe_2 valley polarization.

This fine structure polarization and magnetic field dependence are very similar to results seen in InAs quantum dots[87]. An anisotropic confining potential resulting from an ellipsoidal dot shape leads to an electron-hole exchange interaction which hybridizes the original circularly polarized states[87]. The hybridized states split in energy according to the degree of anisotropy of the confining potential (related to the aspect ratio of the dot), yielding two non-degenerate linearly polarized transitions (Fig. 4.9b). In a magnetic field, strong Zeeman splitting overwhelms the exchange interaction, and the original circularly polarized transitions are recovered (Fig. 4.9d).

In the case of emitters in WSe_2, the original circularly polarized valley states depend on the C_3 rotational symmetry of the lattice. If excitons become confined to an inhomogeneity that does not preserve the C_3 symmetry of the lattice, the inter-valley electron-hole exchange interaction can couple the two circularly polarized transitions to yield linear combinations of the original valley states that are linearly polarized along the symmetry axes of the confining potential (Figure 4.9b)[80,88].

The results measured on CVD WSe_2 are consistent with several reports of narrow emission from exfoliated WSe_2[82–84]. Emitters in exfoliated samples show the same splitting, magnetic field

behavior, and single photon emission, but tend to occur in much lower density. Some studies also report that emitters in exfoliated samples tend to occur at the edges of flakes[81]. Despite this initial interest, the exact nature of the confining potential or defect is still unknown. Rigorous studies correlating the emission with the local lattice structure and density of states will likely be necessary to unambiguously establish this. Far-field optical experiments suffer from diffraction limited resolution however, and typical high-resolution lattice studies via TEM or STM cannot correlate lattice images with optical properties. Despite the lack of material characterization, the observation of single photon emission in WSe_2 monolayers could provide a new application for the 2D materials in developing quantum information and computing technology.

4.6 Electrically-Pumped Emission from Single Defects in WSe_2

One limitation of the initial characterization studies thus far is that they all rely on optical excitation of carriers to observe emission from the single photon emitters in WSe_2. A more direct route relies on electrical injection of electrons and holes into the defect which can potentially enable single photons to be electrically triggered. This is also more appealing from a technological standpoint, since most devices and practical applications rely on electrical control.

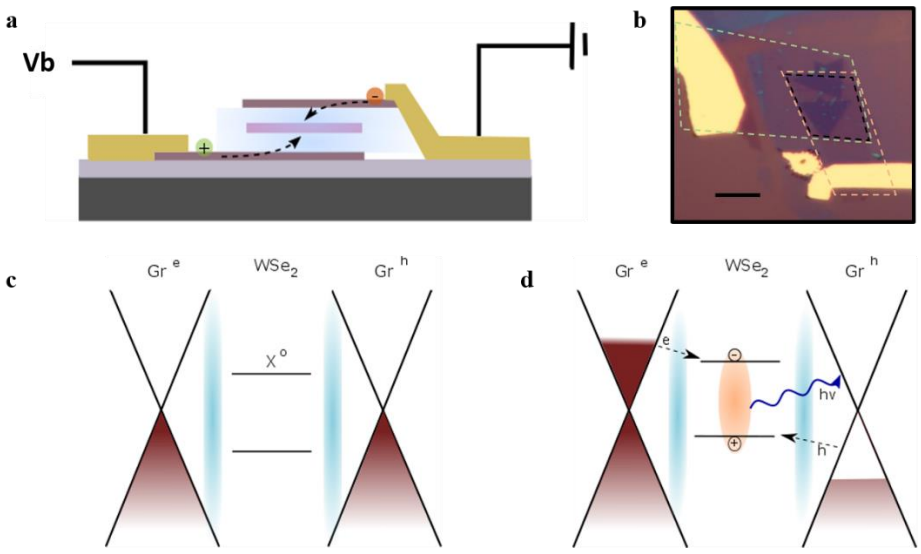

Figure 4.10. **Vertical heterojunction device structure**. **a)** Schematic of vertical heterostructure LED operation. **b)** Optical image of a typical vertical LED. Orange and green dashed lines outline the graphene electrodes, black outlines the device area. Scale bar is 5 μm. **c)** Schematic of device's electronic structure in the unbiased state. X^o denotes neutral intrinsic exciton. **d)** Schematic of device's electronic structure under external bias.

In order to electrically pump the emission from isolated defects, a vertical heterostructure design first demonstrated by Withers *et al.*[89], which allows spatial mapping of EL from intrinsic and defect-bound excitons over a large device area. The vertical device (schematic shown in Fig. 4.10a) consists of two stacked graphene layers as semi-transparent electrodes, separated from a central WSe_2 layer by thin (2-4 layer) hexagonal boron nitride (BN) barriers. For all devices investigated, WSe_2 samples were grown via chemical vapor deposition (CVD), whereas BN and graphene layers were exfoliated from bulk crystals and identified by optical contrast and AFM. The graphene-BN layers have been shown to form tunneling contacts which are nearly independent of temperature. Since the WSe_2 layers were grown via CVD, several independent monolayers can

be integrated into a single heterostructure with an area limited by the exfoliated BN and graphene layers. This not only allows large-active-area LED devices with extremely bright emission, but potentially facilitates investigation of a large number of defects similar to the initial PL characterization studies. Devices were assembled using a polymer film dry-transfer stamping technique described in section 3.2[47]. Figure 4.10b shows an optical microscope image of a device with top and bottom graphene layers outlined in green and orange respectively. The active area defined by their intersection is outlined in black.

4.6.1 *EL from Intrinsic and Defect-Bound Excitons in Vertical Heterojunction Devices*

Injection of electrons and holes into the WSe_2 monolayers relies on the band alignment of the graphene electrodes relative to monolayer WSe_2. Under no external bias, the Fermi level of the graphene layers lies within the band gap of monolayer WSe_2 (Fig. 4.10c). However, as the device is biased (Fig. 4.10d), the Fermi level rises above the available sub-gap defect states. As a result, electrons (holes) can tunnel from the negative (positive) electrode through the thin BN barriers to states in the WSe_2 layers that become accessible as the bias is increased[89]. For 2-4 layer BN tunnel barriers used in these devices, carriers injected from the graphene contacts are expected to remain in the WSe_2 layer and form excitons due to strong Coulomb interactions. Excitons then recombine and lead to electroluminescence (EL) from intrinsic as well as defect-bound exciton states in the WSe_2 layer.

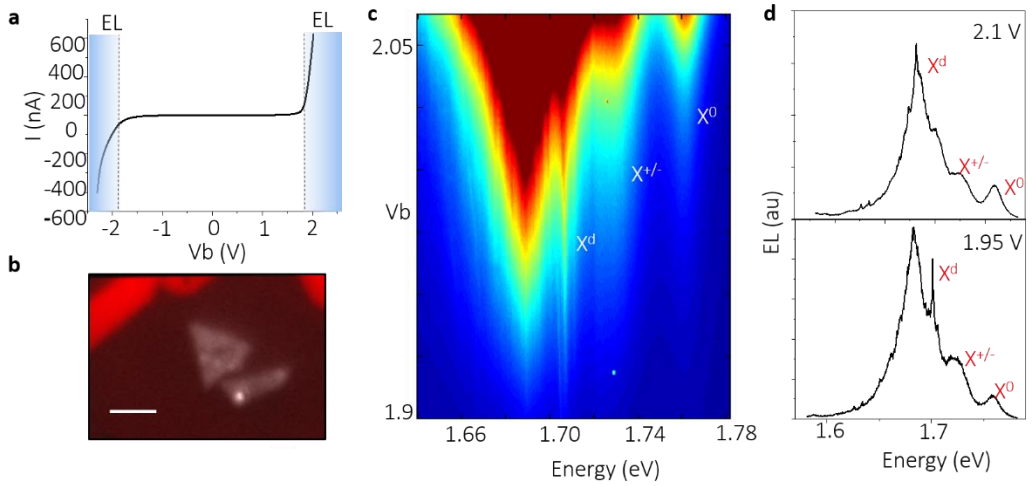

Figure 4.11. **Electroluminescence from heterojunction devices. a)** I/V curve for the device shown in Fig. 4.10b. EL onset is marked by dashed lines at ±1.9 V. **b)** Optical image of EL from the device in Fig. 4.10b under external bias, at a temperature of 5 K. Scale bar is 10 μm. **c)** EL vs. energy and bias voltage, showing evolution of the EL spectrum as the bias voltage is swept to 2.1 V (Color corresponds to EL intensity in linear scale). **d)** Line cuts taken from (c) at 1.95 V and 2.1 V show narrow emission peaks from defect-bound excitons.

Figure 4.11a shows the tunnel current for a typical device as a function of bias voltage V_b, measured at 5 K. The slightly asymmetric I-V_b behavior at positive versus negative bias is likely due to differing thickness in the BN layers, consistent with other reports of asymmetric vertical heterostructure LEDs. At bias values greater than about ±1.9 V, EL is observed from recombination of excitons in the WSe_2 layer and increases in intensity with increasing Vb. At large bias values, bright EL can be observed for all WSe_2 monolayers within the active area of the device, evident in an image of the EL under a bias of 2.1 V (superimposed with a false-color image

of the device, Fig. 4.11b). The near uniform emission from all WSe_2 layers in the active area indicates the spatial homogeneity of the device.

Figure 4.11c shows the evolution of EL as a function of increasing V_b. At bias values between about 1.9 V and 2.0 V, EL is dominated by a broad peak at lower energy than the intrinsic exciton species, 1.651-1.71 eV (marked X^d, Fig. 4.11c and d.). Similar peaks in the PL spectra of WSe_2 are consistent with previous reports of recombination of defect-bound excitons. As the bias is increased above 2 V, peaks emerge in the EL spectrum at 1.72 eV and 1.75 eV, corresponding well with the known energies of the charged and neutral intrinsic excitons respectively. Line cuts taken from the data in Fig. 4.11c at two bias voltages (Fig. 4.11d) show evolution of the EL spectrum as the bias increases. Notably, at low bias, the EL is dominated by defect-bound exciton states (bottom panel, Fig. 4.11d), and a narrow peak at 1.705 eV is visible within the broad continuum of emission between 1.65 eV and 1.71 eV.

4.6.2 *Spatial Mapping and Polarization*

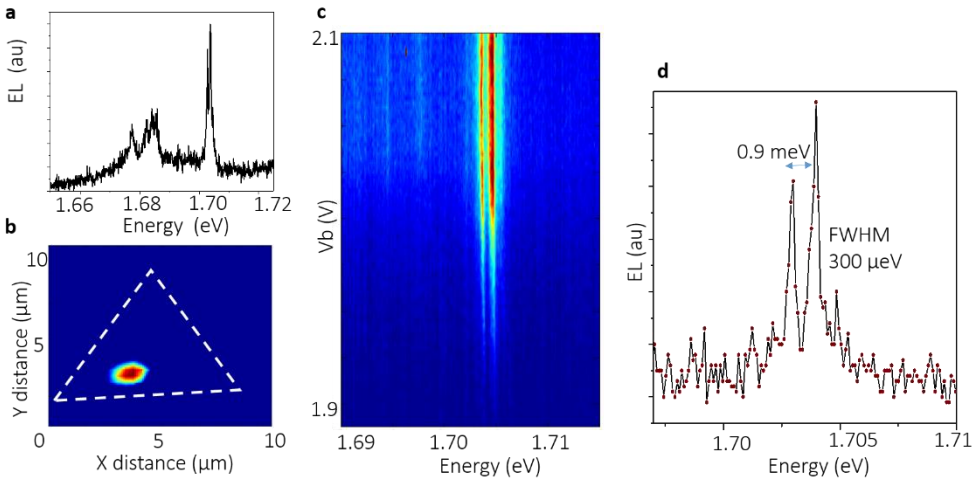

Figure 4.12. **EL from discreet emitters. a)** EL spectrum for a single defect-bound exciton, isolated spatially using a pinhole. **b)** Spatial map of the EL for the spectral

range 1.69 eV to 1.71 eV (Color corresponds to EL intensity in linear scale). **c)** EL from the single defect in Fig. 4.12a as a function of energy and bias. **d)** Line cut from Fig 4.12c at 1.94 V.

Even at low bias values, narrow lines in the EL spectrum are obscured by a broad background of defect emission, not ideal to investigate the specific optical properties of a single peak. In order to isolate single defect EL, a confocal detection method was adopted using a pinhole to isolate emission from a small area of the device at a time. Using this technique (shown in Fig. 4.13a), Fig. 4.12a shows the spectrum of the isolated narrow line at 1.705 eV, which is spatially localized (Fig. 4.12b). The spatially localized EL is distinct from the neutral exciton which is present uniformly across the WSe_2 monolayer. All of the narrow peaks observed in these devices are strongly localized. The narrow emission is electrically controllable as a function of bias voltage (Fig. 4.12c), and can be repeatedly switched on and off by sweeping V_b from 1.9 V to 2.1 V. The peak maintains the same energy and structure for all values of V_b, over repeated bias sweeps.

A line cut taken from Fig. 4.12c at an applied bias of 1.94 V shows that the narrow peak is composed of a fine structure doublet, with two narrow lines (FWHM ~300 μeV) separated by 0.9 meV. All six devices of this kind show similar isolated emitters, which have similar emission characteristics including linewidths on order of several hundred μeV and a doublet structure, where the splitting between the two peaks is in the range of 0.6 meV to 0.9 meV.

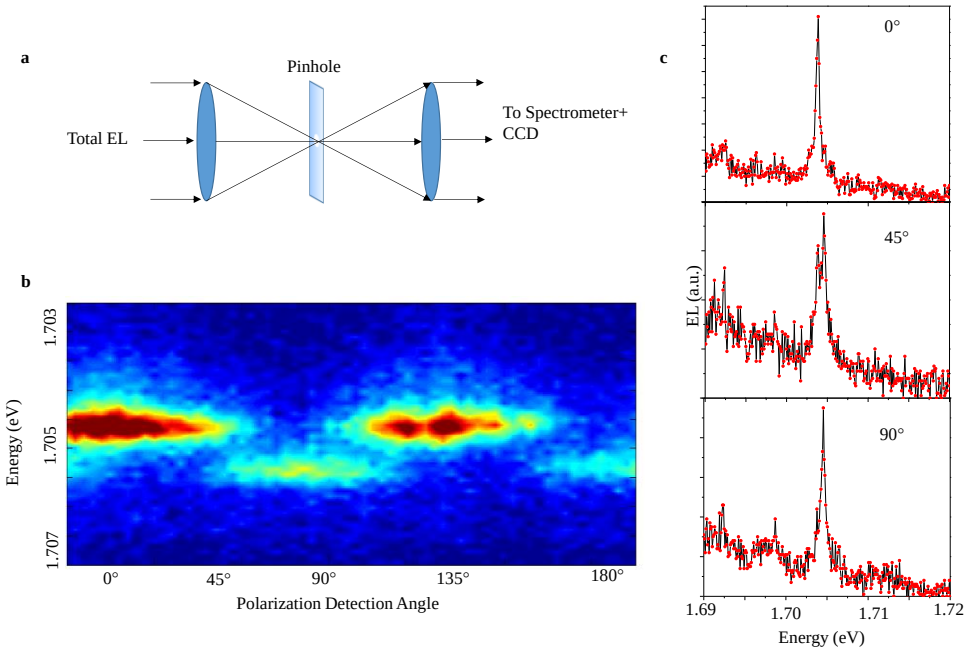

Figure 4.13. **Polarization resolved EL. a)** Schematic of confocal detection method used for isolation of single defects within vertical heterostructure LEDs. A pinhole is used to isolate electroluminescence (EL) from a small spatial region of the device. **b)** EL from a single defect in as a function of energy and polarization detection angle. **c)** Line cuts taken at 0, 45, and 90 degree detection angle show cross linearly polarized transitions consistent with single defect photoluminescence (PL).

Figure 4.13b shows EL from the defect in 4.12 as a function of polarization detection angle and emission energy. Line cuts taken at 0, 45, and 90 degree detection (Fig. 4.13c) show that the doublet is cross linearly polarized, with a near unity degree of polarization.

These spectrally narrow emission lines in the EL spectrum are quantitatively similar to previous reports of PL observed from single photon emitters in WSe_2. PL from the single emitters has linewidth of several hundred μeV with energies 50-100 meV lower than the intrinsic exciton,

and a doublet of cross linearly polarized transitions with average 0.7 meV splitting, all consistent with the observed EL. Since the optical properties of the single photon emitters in WSe_2 arise from the specific defect or impurity causing the confining potential, the high degree of correspondence between the PL and EL implies that the narrow lines are a result of localization to the same type of defect.

4.7 FINAL REMARKS

This work opens up new opportunities to use monolayer WSe_2 for potential applications in optical quantum information, which rely on single photon sources to encode information. Monolayer WSe_2 offers a source of single photons where the emitters are inherently at the surface of the material, potentially enabling significant tunability of the emission, something that is difficult in other solid state single photon sources. Further, it has been demonstrated that it is possible to deterministically pattern arrays of emitters within monolayers, a long sought after goal for single photon generation[90]. Integration of these single emitters in van der Waals LED devices opens applications of WSe_2 in developing on-chip quantum information and nano-photonic technologies, where electrically triggered photon emission is preferable to optically pumped sources.

Chapter 5. WSE_2/CRI_3 HETEROSTRUCTURES FOR SPINTRONIC DEVICES

Both CrI_3 and WSe_2 are unique material systems that have broadened the scope of fundamental studies within 2D materials research to include optical exploration of valley physics and single quantum emitters, as well as studies of two dimensional magnetism. However, one of the most

outstanding features of van der Waals materials is the ease with which they can be combined with other van der Waals layers to form heterostructures that extend their functionality and lead to emergent phenomena[91]. In this chapter I describe heterostructures of monolayer WSe_2 and CrI_3 flakes. These heterostructures enable control of valley pseudospin in WSe_2 through exchange coupling with the CrI_3, as well as spin-dependent charge hopping between the two materials. I then discuss spintronic devices based on bilayer CrI_3 flakes and monolayer WSe_2 that demonstrate a helicity-dependent photocurrent response.

5.1 VAN DER WAALS HETEROSTRUCTURES

Unlike heterostructures formed from traditional 3D materials, which are difficult to controllably grow and suffer from dangling bonds, lattice mismatch, and interfacial inhomogeneity, van der Waals heterostructures can be formed comparatively easily without the need for costly equipment. Given the wide range of physical properties shown by layered materials, this enables considerable freedom to explore interactions between two or more materials with an atomically clean interface. The discovery of an atomically thin layered magnetic material naturally suggests the possibility of creating highly tailorable magnetic van der Waals heterostructures and devices.

A particularly desirable goal, pursued for decades in three dimensional materials, has been the integration of semiconductors with magnetic materials. This is appealing from a technological standpoint, since magnetic materials form the basis for memory and data storage, while semiconductors underpin modern transistor logic. More fundamentally, combining these materials increases the scope of possible "spintronic" devices and enables exploration of interactions between charge carriers in a semiconductor and ordered spins in a magnetic material[1]. Dilute magnetic semiconductors (DMS) such as (Ga,Mn)As and (In,Mn)As formed by introducing

magnetic dopants into well characterized semiconductors, have enabled electrical control of ferromagnetism with critical temperatures as high as 110K[92–94]. Heterostructures formed from DMS layers or magnetic quantum wells have shown spin-polarized resonant tunneling, electrical spin injection, and optical read-out of a tunable spin polarization[95,96]. However, DMS are highly sensitive to defects and impurities that can strongly alter their magnetic behavior, and typically suffer from poor optical quality[92,95]. Heterostructures formed from magnetic quantum wells require highly-controlled growth using MBE, and given the results seen with thin-film magnets, investigation of low-dimensional magnetic behavior in these heterostructures would be impossible. Atomically thin van der Waals materials offer a means to combine semiconductor functionality with layer-dependent two-dimensional magnetism, without sacrificing the properties or integrity of either component. These heterostructures can be fabricated using the procedure described in chapter 2 section 3, used to prepare gated CrI_3 devices.

5.2 Interfacing Monolayer WSe_2 with CrI_3

Among the available van der Waals materials, the well-studied MX_2 semiconductors provide an obvious choice to combine with CrI_3. They show fundamentally interesting and optically accessible spin-dependent physics that can potentially interact with, and be controlled by, the magnetic spins in CrI_3. Tungsten Diselenide (WSe_2) in particular is well-suited to interface with CrI_3.

Like other TMD materials, WSe_2 shows well-characterized valley-dependent optical selection rules (See section 4.1) enabling initialization of exciton populations from each valley, based on the circular polarization state of the excitation vs collection (ie σ+ excitation prepares a population of excitons in the K+ valley, while σ- excitation creates excitons in the K-). Low

temperature PL studies have shown that inter-valley scattering times are typically longer than the radiative lifetime of excitons, meaning that excitons retain their polarization state upon radiative recombination and their valley pseudospin can be optically read-out through the polarization of their PL[61,78,97]. High optical quality WSe_2 flakes typically show well defined excitonic species at low temperature, with valley polarization > 50%[78].

Beyond the ability to initialize and optically read out valley pseudospin, for any further applications the ability to lift the degeneracy between the two valleys is desirable. Interaction with a magnetic field offers a potential means of accomplishing this, since the sign of the angular momentum is opposite for the two valleys. This has been demonstrated in a number of studies on the valley Zeeman Effect in WSe_2 using external magnetic fields applied along the c-axis of the WSe_2 layer (the axis of spin quantization in WSe_2)[85,86,98,99].

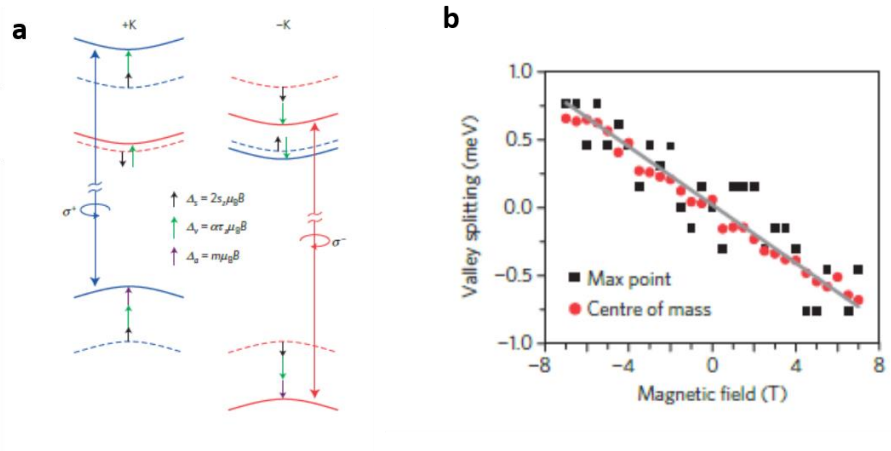

Figure 5.1. **Valley Zeeman effect in monolayer WSe_2. a)** +K and –K valleys without (solid lines) and with (dashed lines) an external magnetic field. Black, green, and purple arrows show contributions from spin, valley, and orbital magnetic moment to the observed valley Zeeman shift. **b)** Valley splitting vs applied magnetic field.

Figure 5.1a shows a band diagram for valley excitons in WSe_2 with (solid lines) and without (dashed lines) an external magnetic field[85]. The purple, blue, and black arrows show angular momentum contributions to the energy shift for conduction and valence bands in the presence of an external field. Since the observed energy for the K and -K valley excitons depends on conduction-valence band separation, the real spin (black arrows) does not contribute to any valley-dependent shift in a magnetic field. The atomic orbital and valley orbital momenta do contribute to an observed valley Zeeman shift however, since their sign is reversed between the two valleys. The result is an observed linear energy splitting of 0.1-0.2 meV/T between the energies of excitons in the K and -K valleys (Fig. 5.1b). This shows that magnetic field is a promising means of controlling valley pseudospin in devices and heterostructures, but a large external field is needed to achieve even modest energy splitting between the two valleys.

5.3 Controlling Valley Psuedospin in CrI_3/WSe_2 Heterostructures

A van der Waals heterostructure involving a magnetic substrate enables the use of proximity-induced magnetic exchange effects to generate very strong coupling with magnetic spins in the substrate. While proximity-induced magnetic exchange is typically considered a weak effect in bulk samples, this surface effect has the potential to significantly alter the electronic behavior of an atomically thin layer[100,101]. Applied to WSe_2, it could potentially result in much larger effective magnetic fields in the WSe_2 layer and large valley energy splitting, without applying external magnetic fields. Strong proximity-induced magnetic exchange effects have been demonstrated in a number of other van der Waals materials using bulk magnetic substrates, including graphene on EuS substrates[102,103]. Recently this has also been successfully observed in heterostructures of monolayer WSe_2 and ~10nm CrI_3 flakes[104].

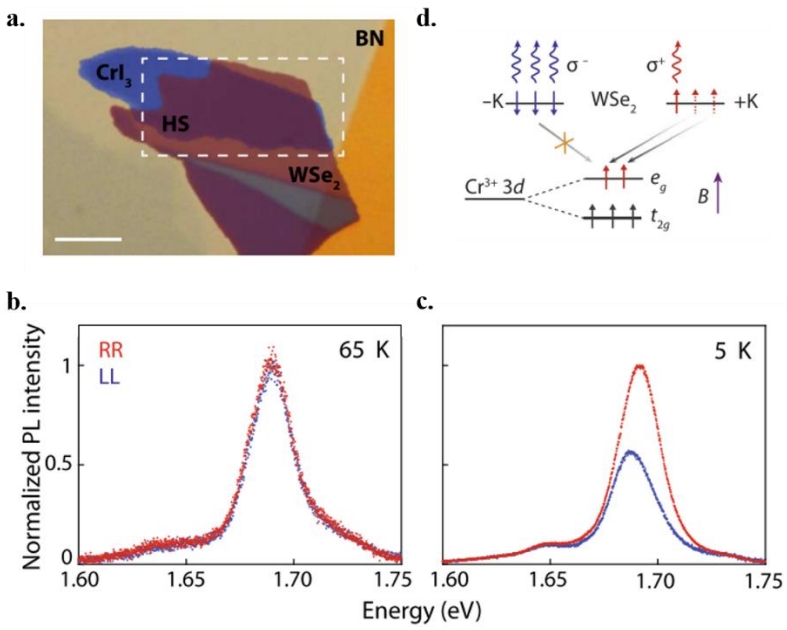

Figure 5.2. **PL characterization of heterostructures. a)** False-color microscope image of a finished heterostructure. **b)** Circular polarization-resolved PL spectra taken on the heterostructure at 65K. **c)** Circular polarization-resolved PL spectra taken on the heterostructure at 5K. Taken from reference 104.

Figure 5.2a shows a false-color optical microscope image of a van der Waals heterostructure comprised of monolayer WSe_2 and a ~10nm CrI_3 flake. The heterostructure region (labeled "HS") is outlined by the dashed white line. Due to the moisture sensitive nature of the CrI_3 layer, thicker hBN layers are used to encapsulate the heterostructure (light and dark yellow regions), and do not affect the optical or magnetic properties of the structure[104]. Figure 5.2b shows polarization-resolved PL spectra taken on the heterostructure at 65K, above the curie temperature of the CrI_3. The red curve corresponds to right circularly polarized (RCP) excitation and detection of RCP emission, while the black curve corresponds to left circularly polarized (LCP) excitation and detection of LCP emission. The red curve measures co-polarized emission from an exciton population prepared in the +K valley (measured through excitation and detection of right

circularly-polarized light, RR), while the black curve measures emission from excitons residing in the -K valley (measured through excitation and detection of left circularly-polarized light, LL). Figure 5.2c shows the same measurement taken at the same spot on the heterostructure, at a temperature of 5K well below the Curie temperature of the CrI_3. While the RR and LL spectra are virtually identical above the Curie temperature, at 5K they show a significant difference in peak energy as well as a difference in intensity. The energy splitting between the two valleys is about 3.5 meV, which corresponds to an effective field of about 13T. This large valley splitting is ascribed to lifting of the valley degeneracy resulting from exchange interactions between the WSe_2 excitons and the CrI_3 layer as it spontaneously magnetizes below its Curie temperature[104]. Like in the valley Zeeman effect observed in WSe_2 monolayers in external magnetic fields, this shift in the energy of exciton emission from the two valleys arises from distinct coupling effects in the valence vs conduction bands.

Another striking feature of the PL spectra in figure 5.2c is the large difference in total PL intensity between the RR and LL curves. This is the case even though there is no difference in absorption of RCP vs LCP light at the excitation energy (633nm). CrI_3 is a ferromagnetic semiconductor, and so band alignment between the CrI_3 and WSe2 plays a large role in the optical properties of the heterostructure. The alignment between WSe_2 and CrI_3 is predicted to be type II[104], with the lowest unoccupied CrI3 orbital (the e_g orbital) lying below the WSe_2 conduction band (figure 5.2d). However, these orbitals are spin-polarized e_g orbitals, meaning that charge hopping of electrons from WSe_2 into the CrI_3 e_g states should only occur for electrons of the correct spin orientation. Due to the spin-valley locking in WSe_2, RCP excitation creates $|K,\uparrow\rangle$ electrons, while LCP excitation creates $|-K,\downarrow\rangle$ electrons. This means that only electrons from a specific valley can hop into the CrI_3 eg orbitals depending on their spin polarization, which derives from

the magnetic orientation of the CrI_3. As a result, there is an extra non-radiative channel for one valley compared to the other, leading to less observed PL from the valley with the additional non-radiative channel. This is also supported by the fact that the energy of the WSe_2 PL peak observed on the heterostructure corresponds fairly well with that of the positive trion state, indicating significant charge transfer between CrI_3 and WSe_2 leading to an excess of holes left in the WSe_2.

5.4 Spintronic Devices from CrI_3/WSe_2 Heterostructures

These results demonstrate the power of two-dimensional materials and their heterostructures to achieve precise control over charge, spin, and pseudospin through extremely strong interfacial interactions unattainable in bulk materials. The unique combination of spin and valley pseudospin magnetic control present in CrI_3/Wse_2 heterostructures, combined with their type II band alignment, makes them ideal candidates for spintronic devices. In particular, the spin dependent charge hopping from WSe_2 to CrI_3 suggests a potential spin-dependent photovoltaic effect. Since the charge-hopping rate is large when the photo-excited spin is aligned with the magnetization in CrI_3 and small in the anti-aligned condition, photocurrent through the device should have a strong dependence on the excitation helicity. Any photocurrent through the device can be switched on and off when the photo-excited spin is aligned and anti-aligned with the CrI_3 magnetization, respectively.

A direct application of this spintronic device would be as a polarization sensitive photodetector. Graphene and MX_2 semiconductors have been successfully used as the active material in photodetectors with a significant spectral range. However, a polarization dependent response has been less straight-forward to achieve. Yuan *et al.* demonstrated a photodetector sensitive to linear polarization based on bulk flakes of black phosphorous[105]. Their device takes advantage of the strong in-plane structural anisotropy and resulting anisotropic absorption of black

phosphorus, since the observed photo-response depends very strongly on the efficiency of absorption of the excitation. Their device would be unable to distinguish between RCP and LCP excitation, however.

5.5 Device Operation and Optical Characterization

In order to study the polarization-dependent photocurrent from WSe2/CrI_3 heterostructures, a vertical diode structure is ideal, to take advantage of the built-in field at the heterostructure interface and allow a large active area. Figure 5.3a shows a cartoon of a simplified device structure. Graphene provides a transparent conducting layer at the top and bottom of the device, separated from the central heterostructure by few-layer hBN tunneling barriers (typically trilayer BN is an ideal thickness). A lithographically patterned gold contact allows external contact to the device. Devices were fabricated using a dry transfer technique described in detail in chapter 3, in which the device components are sequentially picked up from SiO2 substrates onto a PDMS+Polycarbonate stamp, and deposited onto the bottom layer of hBN. Due to the moisture sensitive nature of CrI_3, all transfers were carried out under inert atmosphere in a glovebox. The finished devices, encapsulated in thick hBN layers, could then be removed from the glovebox for lithography and wire-bonding. Figure 5.3b shows an optical microscope image of a finished device with patterned gold contacts. The blue dashed line marks the CrI_3 flake, while the orange dashed line marks the WSe_2 layer. The shaded area corresponds to the heterostructure.

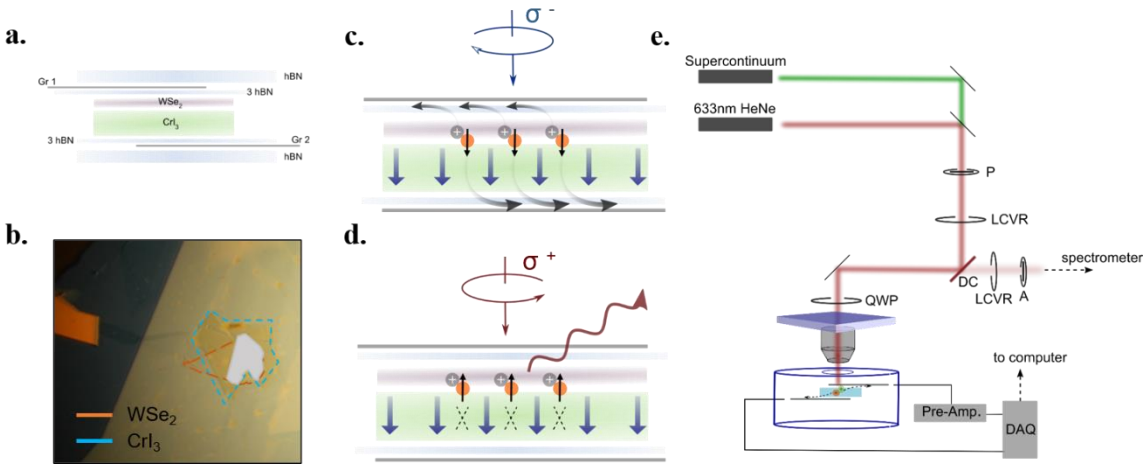

Figure 5.3. **Vertical tunneling diode device based on WSe_2/CrI_3 heterostructures. a)** Cartoon of vertical tunneling diode device based on WSe_2/CrI_3 heterostructures. **b)** Optical microscope image (100x) of a completed device. Blue dashed line outlines the CrI_3 flake, orange outline corresponds to the WSe_2 layer. The shaded region is the active area of the device. **c)** Expected device operation for σ- excitation and a CrI_3 flake magnetized in the spin-down orientation. **d)** Device operation for the same CrI_3 orientation under σ+ excitation. **e)** Cartoon depicting the optical and electrical setup used to measure photocurrent and PL.

Expected device operation is shown in figures 5.3c and 5.3d, for a device with a CrI_3 flake magnetized in the spin-down orientation. Excitation with LCP (σ-) light of the appropriate wavelength populates the WSe_2 –K valley conduction band with $|-K,\downarrow\rangle$ electrons. These electrons can then hop to the spin-down polarized e_g orbitals in the CrI_3 and be collected by the bottom graphene contact, while holes remain in the WSe_2 layer. This leads to an observed photocurrent through the device, and significantly reduced σ- photoluminescence. Excitation with RCP (σ+) light however (fig. 5.3d), creates $|+K,\uparrow\rangle$ electrons in the WSe_2 +K valley. Since their spin is oppositely oriented to that of the e_g orbitals, charge hopping to the CrI_3 layer is prevented.

In this case very little photocurrent should be observed, while the σ+ photoluminescence should be large.

In order to characterize the optical and electrical response of the devices, photoluminescence and photocurrent measurements are taken using an optical and electrical setup shown in Figure 5.3e. Optical excitation is provided by a continuous wave (CW) HeNe laser at 633nm, a tunable pulsed supercontinuum source (500-1000), or a tunable CW Ti:Saph source (700-1000nm) depending on the nature of the measurements. For polarization resolved PL and photocurrent, circularly polarized light is generated using a linear polarizer, liquid crystal variable retarder (LCVR) functioning as a half-wave plate, and a quarter wave plate. Circularly polarized emission is analyzed using the same quarter wave plate, in combination with an LCVR and analyzer in the collection path. A dichroic beam splitter is used to separate the excitation path from the collection path. The incident beam is focused onto the sample at normal incidence using a 40X objective mounted on a piezoelectric scanning stage, and PL is collected using the same objective. The scanning objective allows spatially resolved photocurrent and PL measurements. The sample is housed in a closed-cycle helium cryostat at a base temperature of 5K, and an external magnetic field can be applied in Faraday geometry using a superconducting magnet external to the cryostat. Kerr rotation measurements to characterize the magnetic behavior of the CrI_3 layer were also carried out as described in an earlier section. Photocurrent is measured using a National Instruments DAQ and a current pre-amplifier.

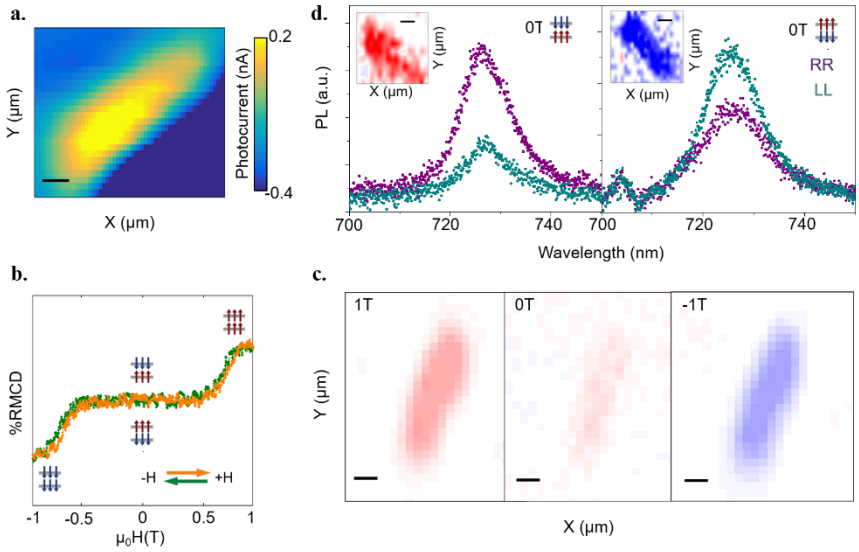

Figure 5.4. **Optical characterization of WSe_2/CrI_3 heterostructures. a)** Spatial map of photocurrent under 633nm excitation (power is 4 μW, scale bar is 2μm). **b)** %RMCD (equivalent to Kerr rotation) as a function of applied magnetic field, measured at a single spot on the heterostructure. **c)** Spatial maps of %RMCD over the entire heterostructure at select magnetic fields. Scale bar is 2μm. **d)** PL spectra taken on the heterostructure at 0T, for the AF and AF' anti-aligned spin states. Insets show spatial maps of the polarization dependence of the photoluminescence for each state (scale bar is 2μm).

Figure 5.4a shows a spatial map of the photocurrent at zero applied bias from a device using a bilayer CrI_3 flake with 633nm cw excitation at 4 uW. The yellow central region of positive current corresponds to photocurrent observed on the heterostructure. The adjacent region of strong negative photocurrent is off of the heterostructure and likely results from carriers in the WSe_2 and graphene electrodes alone (it is ignored in further measurements). In all measurements, photocurrent is measured at the WSe_2 electrode, and the positive sign suggests hole transfer to the

WSe_2 layer and electron transfer to the CrI_3, as predicted for the type-II band alignment between the WSe_2 and CrI_3 layers.

In order to establish the magnetic states of the CrI_3 layer, field-dependent RMCD measurements were taken similar to those described in part 1. Figure 5.4b shows %RMCD as a function of external field, measured at a single spot on the heterostructure. Since WSe_2 is not magnetic, all RMCD signal is assumed to arise from the CrI_3. Consistent with all other measured bilayers, the flake shows zero net RMCD at fields less than about ±0.6T, with the two layers antiferromagnetically aligned in one of two possible states. At fields greater than ±0.6T, the layers are aligned and a large positive or negative RMCD is observed. Field-dependent spatial maps taken at 1, 0, and -1 T (Fig. 5.4 c) show the homogenous magnetic behavior of the flake, with no observable domains or inhomogeneity.

Polarization-resolved photoluminescence measurements taken at 0T reveal a large intensity difference between right and left circularly polarized emission (Fig. 5.4d). The right panel shows PL data taken at 0T when the bilayer is in the AF configuration (ie top layer is spin-up). In this case, left circularly polarized emission is significantly stronger than right. A spatial map over the flake (inset) reveals that this is true for the entire flake, and is not the result of a location-dependent phenomenon. Conversely, in the AF' state corresponding to the top layer being spin-down (left panel), right circularly polarized emission is significantly stronger than left. While this intensity difference is consistent with the results from heterostructures containing 5-10nm thick CrI_3 flakes, their behavior is assumed to be simply ferromagnetic. In bilayer flakes, the two layers have opposite spin orientation. Given that there is still evidence for significant spin-dependent charge transfer between WSe_2 and CrI_3, and that the polarization dependence of this is reversed for the two anti-aligned spin configurations (Fig. 5.4d, right vs left panel), it seems as though

charge transfer occurs preferentially to the topmost layer of the CrI_3. This is consistent with results from WSe_2/bilayer CrI_3 heterostructures measured in other studies (Zhong, D *et al.*, in preparation).

5.6 Helicity Dependent Photocurrent

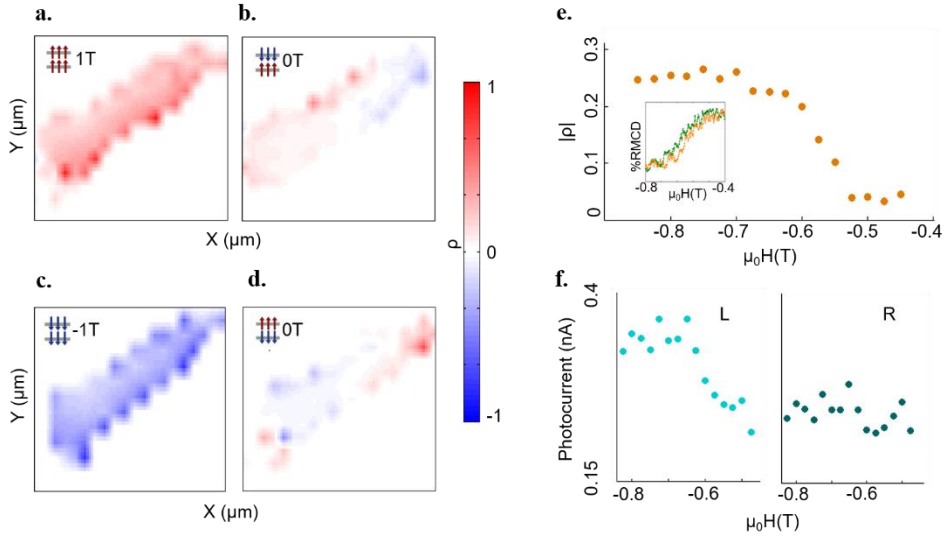

Figure 5.5. **Helicity dependent photocurrent. a-d)** Spatial maps of ρ taken at select field values. Scale bar is 2μm **e)** Evolution of |ρ| as the applied field is swept from -0.45T to -0.85T. Inset shows the %RMCD for the same field values. **f)** Evolution of the magnitude of the photocurrent over the same field values as shown in e), under RCP (right panel) and LCP (left panel) excitation.

The photocurrent also shows a pronounced dependence on the excitation polarization and the magnetic state of the CrI_3. Figure 5.5a-d shows the evolution of the normalized photocurrent polarization ρ, defined as $(PC_R - PC_L)/|\min(PC_R, PC_L)|$, for the entire flake at select magnetic fields . At 1T when the CrI_3 bilayer is in a spin-aligned state (Fig. 5.5a), ρ is ~0.25 for the entire flake, meaning that there is significantly more photocurrent observed when exciting with right circularly polarized light vs with left. When the field is swept down to 0T (Fig. 5.5b) and the CrI_3

spins in each layer are anti-aligned, |ρ| decreases to ~0.05, for the entire flake. Interestingly, there are two domains clearly visible on the flake, one with a positive polarization ($PC_R > PC_L$) and one with negative ($PC_L > PC_R$). At -1T (Fig. 5.5c), the spins of the CrI_3 bilayer are aligned in the spin-down orientation, and ρ is now uniformly ~ -0.25 over the entire flake, meaning that the photocurrent with LCP excitation is now significantly larger than the photocurrent with RCP excitation. Upon sweeping the field back up to 0T (Fig. 5.5d), |ρ| again decreases to ~ 0.05, and the same domain pattern emerges, now with the spatial dependence of the sign of ρ reversed. The spin-dependence of the charge transfer observed at 0T in the PL is uniform over the entire flake (Fig. 5.5d insets), and the RMCD observed at 0T is vanishingly small and uniform over the entire flake. This domain pattern is only observable in the photocurrent, and its origin is as yet unknown.

Figure 5.5 e shows the evolution of |ρ| as the applied magnetic field decreases from -0.45T to -0.85T. The inset shows the corresponding evolution of the RMCD for the same field values. As the field decreases below about -0.55T, |ρ| rapidly increases from about 0.05, consistent with the value seen at 0T (Fig. 5.5 b,d) to about 0.25, consistent with the values seen at ±1T (Fig. 5.5 a,c). The field-dependent behavior also closely follows the evolution of the RMCD signal as a function of external field (inset). This is also the case for positive field values (not shown). The polarization dependence of the photocurrent appears strongly tied to the magnetic state of the CrI_3, consistent with the predicted behavior of this type of device. However, the antiferromagnetic inter-layer coupling in bilayer CrI_3 adds an additional complicating factor to the observed behavior of the device.

One potential contribution to the observed polarization dependence of the photocurrent could arise from the spin-dependent charge hopping between the two layers. At -1 and 1T, spins in both layers of the CrI_3 are aligned with the external field. Photo-excited electrons in WSe_2 of

the appropriate spin can hop into the CrI_3, primarily into the top layer (consistent with the 0T PL measurements). Since the spins in the second CrI_3 layer have the same orientation as the first, these transferred electrons can also travel through the second CrI_3 layer into the graphene electrodes, resulting in photocurrent. Photo-excited electrons in the WSe_2 of the opposite spin orientation cannot hop into either CrI_3 layer, and so a pronounced polarization dependence is observed in the photocurrent. However, at external fields less than ±0.6T, the bottom layer of the CrI_3 has an opposite spin orientation to the top. Electrons in the WSe_2 with the appropriate spin can hop into the top layer of the CrI_3, however tunneling from the first through the second layer of the CrI_3 into the bottom graphene electrode should be impossible. Electrons of the opposite spin orientation still cannot hop into the top layer of the CrI_3.

Considering only these factors, there should be no photocurrent observable for either excitation polarization when the bilayer is in the antiferromagnetic state. Figure 5.5f shows the evolution of the magnitude of the photocurrent for RCP (right panel) and LCP (left panel) excitation as a function of external field. At -0.85T, there is a large difference in the magnitude of photocurrent with RCP vs LCP excitation, as expected. As the magnitude of the applied field decreases however, only LCP photocurrent shows a strong dependence on the field. As the field approaches -0.45, it shows a pronounced decrease and approaches a value roughly equal to the RCP photocurrent. The RCP photocurrent fluctuates randomly and shows no discernable dependence on field. Photocurrent is still observed at 0T however, and has a small, spatially dependent polarization, the origin of this helicity dependence at 0T is unknown.

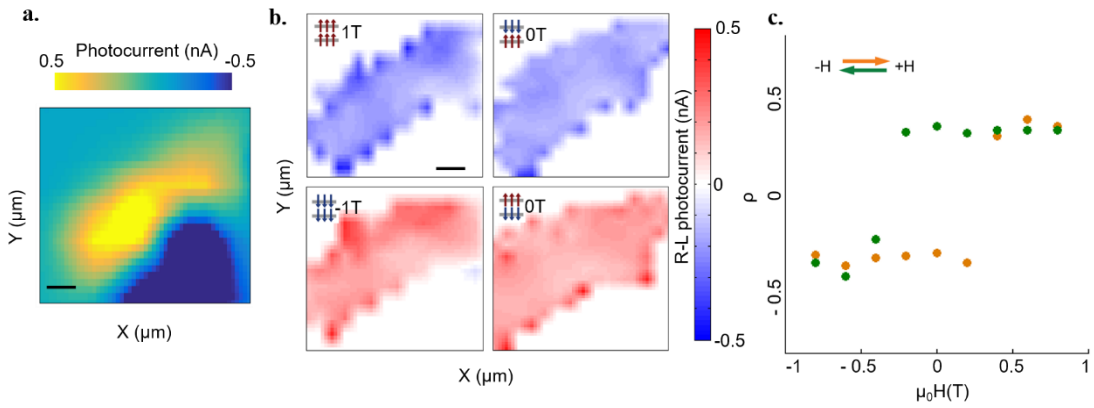

Figure 5.6. **Helicity dependent photocurrent at 730nm. a)** Spatial map of the photocurrent under 730nm excitation (power is 4μW, scale bar is 2μm). **b)** Spatial maps of ρ taken at select field values. Scale bar is 2μm. **c)** Evolution of ρ as the applied field is swept from 0.85T to -0.85T (green dots) and from -0.85T to 0.85T (orange dots).

In addition to observing the behavior of the photocurrent as a function of the external field and excitation polarization, it is also possible to vary the energy of the excitation. As an initial investigation, photocurrent was measured using 730nm excitation, below resonance with the WSe_2 exciton, and also below the emission energy of the PL measured for this heterostructure (Fig. 5.4d). Figure 5.6a shows a map of the total photocurrent at 730nm excitation (still 4μW) at 0T. There is still significant observable photocurrent and the sign of the photocurrent is positive, suggesting that electrons are still transferred to the CrI_3 and holes remain in the WSe_2 layer. However, the polarization dependence of the photocurrent with 730nm excitation is entirely different than with 633nm excitation. Figure 5.6b shows spatial maps of ρ at 1, 0, and -1T similar to Figure 5.5 a-d. Now, at 1T ρ is about -0.35 over the entire flake. Not only is the magnitude of the photocurrent polarization larger than with 633nm excitation, but the sign is reversed ie at 633nm $PC_R > PC_L$,

while at 730nm $PC_L > PC_R$. When the field is swept from 1T to 0T, the polarization of the photocurrent is maintained and ρ is still about -0.35 over the entire flake. At -1T, the polarization switches sign, and is approximately 0.35. This polarization is also maintained upon sweeping the field back to 0T. Figure 5.6c shows field-dependent behavior of ρ as the field is swept from 0.85T to -0.85T (green dots) and back up to 0.85T (yellow dots). The behavior of ρ is now ferromagnetic, with a clear hysteresis loop centered about 0T and a coercive field of approximately 0.3T. This is in contrast to the antiferromagnetic behavior observed in all studies of bilayer CrI_3 using 633nm excitation. The spatial maps in Figure 5.6b showing significant polarization retained at 0T support the fact that the behavior of ρ is now ferromagnetic, and demonstrate that this effect is present over the entire heterostructure. The origin of this switch in behavior from antiferromagnetic to ferromagnetic is as yet unknown.

An additional contribution to the observed helicity dependence of the photocurrent could arise from helicity dependence in the absorption of both the CrI_3 and WSe_2 layers. Preliminary white light absorption measurements have shown that CrI_3 shows helicity-dependent absorption peaks, which could lead to larger photocurrent when exciting with the helicity that is more strongly absorbed by the CrI_3 bilayer. Furthermore, the WSe_2 absorption peak near 725nm should show a Zeeman shift between the two spin polarizations, meaning that for near-resonant or resonant excitation, the WSe_2 layer also shows helicity-dependent absorption. However, in this case, due to the short spatial extent of the exchange coupling, the shift should follow the orientation of the top layer of the bilayer only. This could potentially explain the appearance of a hysteresis loop observed in the helicity dependence of the photocurrent for excitation at 730nm.

5.7 Final Remarks

These measurements show that heterostructures of CrI_3 and WSe_2 are promising candidates for realizing spintronic devices based on 2D van der Waals magnetic materials. In addition to utilizing the magnetic properties of the CrI_3 to achieve control of valley pseudospin in monolayer TMD materials[104], the interaction between the two materials due to band alignment and resulting charge hopping can be utilized to achieve novel spintronic device structures. The band offset between the WSe_2 conduction band and lowest unoccupied CrI_3 orbitals results in charge transfer upon optical excitation, leading to significant photocurrent without the need for external bias across the heterostructure. Furthermore, since the orbitals in the CrI_3 are spin-polarized below its Curie temperature, the photocurrent shows significant helicity dependence, ideal for a variety of applications including photodetectors. Beyond the devices discussed here, it remains to be explored whether the electron hopping from the WSe_2 to the CrI_3 effects the magnetic behavior of the CrI_3. This could be used for optical control of magnetic behavior in CrI_3 flakes, potentially desirable for more rapid control of magnetic behavior then can be attained using gate voltage, described in Chapter 3.

BIBLIOGRAPHY

1. Wolf, S. A. and Awschalom, D. D. and Buhrman, R. A. and Daughton, J. M. and von Molnar, S. and Roukes, M. L. and Chtchelkanova, A. Y. and Treger, D. M. Spintronics: a spin-based electronics vision for the future. *Science* **294,** 1488–95 (2001).

2. Peierls, B. Y. R. on Ising ' S Model of Ferromagnetism. *Math. Proc. Cambride Philos. Soc.* **31,** 477–481 (1936).

3. Onsager, L. Crystal statistics. I. A two-dimensional model with an order-disorder transition. *Phys. Rev.* **65,** 117–149 (1944).

4. Liu, B., Zou, Y., Zhang, L., Zhou, S., Wang, Z., Wang, W., Qu, Z. & Zhang, Y. Critical behavior of the quasi-two-dimensional semiconducting ferromagnet CrSiTe 3. *Sci. Rep.* **6,** 2–9 (2016).

5. Staunton, J. B. Reports on Progress in Physics Related content The GW method. (1998).

6. Wilson, K. G. Problems in Physics with many Scales of Length. *Sci. Am.* **241,** 158–179 (1979).

7. De Jongh, L. J. & Miedema, a. R. Experiments on simple magnetic model systems. *Adv. Phys.* **23,** 1–260 (1974).

8. Samarth, N. Condensed-matter physics: Magnetism in flatland. *Nature* **546,** 216–218 (2017).

9. Mermin, N. D. & Wagner, H. Absence of ferromagnetism or antiferromagnetism in one- or two-dimensional isotropic Heisenberg models. *Phys. Rev. Lett.* **17,** 1133–1136 (1966).

10. Bruno, P. Absence of Spontaneous Magnetic Order at Nonzero Temperature in One- and Two-Dimensional Heisenberg and XY Systems with Long-Range Interactions. *Phys. Rev. Lett.* **87,** 137203 (2001).

11. Rau, C. Ferromagnetic order and critical behavior at surfaces of ultrathin epitaxial films. *Appl. Phys. A Solids Surfaces* **49,** 579–587 (1989).

12. Li, Y. & Baberschke, K. Dimensional crossover in ultrathin Ni(111) films on W(110). *Phys. Rev. Lett.* **68,** 1208–1211 (1992).

13. Ballentine, C. a., Fink, R. L., Araya-Pochet, J. & Erskine, J. L. Magnetic phase transition in a two-dimensional system: p(1 x 1)-Ni on Cu(111). *Phys. Rev. B* **41,** 2631–2635 (1990).

14. Huang, F., Kief, M. T., Mankey, G. J. & Willis, R. F. Magnetism in the few-monolayers limit: A surface magneto-optic Kerr-effect study of the magnetic behavior of ultrathin films of Co, Ni, and Co-Ni alloys on Cu(100) and Cu(111). *Phys. Rev. B* **49,** 3962–3971 (1994).

15. Shirane, G. J . *Phys. Rev. Lett.* **22,** 1–4 (1969).

16. Birgeneau, R. J., Guggenheim, H. J. & Shirane, G. Neutron Scattering Investigation of Phase Transitions and Magnetic Correlations in the Two-Dimensional Antiferromagnets K2NiF4, Rb2MnF4, Rb2FeF4. *Phys. Rev. B* **1,** 2211–2230 (1970).

17. Splendiani, A., Sun, L., Zhang, Y., Li, T., Kim, J., Chim, C. Y., Galli, G. & Wang, F. Emerging photoluminescence in monolayer MoS2. *Nano Lett.* **10,** 1271–1275 (2010).

18. Mak, K. F., Lee, C., Hone, J., Shan, J. & Heinz, T. F. Atomically Thin MoS_2: A New Direct-Gap Semiconductor. *Phys. Rev. Lett.* **105,** 136805 (2010).

19. Novoselov, K. S., Geim, a K., Morozov, S. V, Jiang, D., Katsnelson, M. I., Grigorieva, I. V, Dubonos, S. V & Firsov, a a. Two-dimensional gas of massless Dirac fermions in graphene. *Nature* **438,** 197–200 (2005).

20. Lin, M. W., Zhuang, H. L. L., Yan, J. Q., Ward, T. Z., Puretzky, a a, Rouleau, C. M., Gai, Z., Liang, L. B., Meunier, V., Sumpter, B. G., Ganesh, P., Kent, P. R. C., Geohegan, D. B., Mandrus, D. G. & Xiao, K. Ultrathin nanosheets of CrSiTe3: a semiconducting two-dimensional ferromagnetic material. *J. Mater. Chem. C* **4,** 315–322 (2016).

21. Casto, L. D., Clune, a. J., Yokosuk, M. O., Musfeldt, J. L., Williams, T. J., Zhuang, H. L., Lin, M. W., Xiao, K., Hennig, R. G., Sales, B. C., Yan, J. Q. & Mandrus, D. Strong spin-lattice coupling in CrSiTe3. *APL Mater.* **3,** (2015).

22. Kim, H.-S. & Kee, H.-Y. Crystal structure and magnetism in $RuCl_3$: An *ab initio* study. *Phys. Rev. B* **93,** 155143 (2016).

23. Sandilands, L. J., Tian, Y., Plumb, K. W., Kim, Y. J. & Burch, K. S. Scattering Continuum and Possible Fractionalized Excitations in RuCl3. *Phys. Rev. Lett.* **114,** (2015).

24. Kim, H.-S., V., V. S., Catuneanu, A. & Kee, H.-Y. Kitaev magnetism in honeycomb $RuCl_3$ with intermediate spin-orbit coupling. *Phys. Rev. B* **91,** 241110 (2015).

25. Le Flem, G., Brec, R., Ouvard, G., Louisy, a. & Segransan, P. Magnetic interactions in the layer compounds MPX3 (M = Mn, Fe, Ni; X = S, Se). *J. Phys. Chem. Solids* **43,** 455–461 (1982).

26. Chittari, B. L., Park, Y., Lee, D., Han, M., MacDonald, A. H., Hwang, E. & Jung, J. Electronic and magnetic properties of single-layer MPX_3 metal phosphorous trichalcogenides. *Phys. Rev. B.* 1–16 (2016).

27. Handy, L. L. & Gregory, N. W. A Study of the Chromous-Chromic Iodide Equilibrium. *J. Am. Chem. Soc.* **72,** 5049–5051 (1950).

28. Dillon, J. F. & Olson, C. E. Magnetization, resonance, and optical properties of the ferromagnet CrI3. *J. Appl. Phys.* **36,** 1259–1260 (1965).

29. McGuire, M. a., Dixit, H., Cooper, V. R. & Sales, B. C. Coupling of crystal structure and magnetism in the layered, ferromagnetic insulator cri3. *Chem. Mater.* **27,** 612–620 (2015).

30. Zhang, W.-B., Qu, Q., Zhu, P. & Lam, C.-H. Robust intrinsic ferromagnetism and half semiconductivity in stable two-dimensional single-layer chromium trihalides. *J. Mater. Chem. C* **3,** 12457–12468 (2015).

31. Wang, H., Eyert, V. & Schwingenschlögl, U. Electronic structure and magnetic ordering of the semiconducting chromium trihalides CrCl 3 , CrBr 3 , and CrI 3. *J . Phys . Condens . Matter* **23,** 116003–8 (2011).

32. Sivadas, N., Okamoto, S. & Xiao, D. Gate-controllable magneto-optic Kerr effect in layered collinear antiferromagnets. **1,** 1–5 (2016).

33. Lee, J.-U., Lee, S., Ryoo, J. H., Kang, S., Kim, T. Y., Kim, P., Park, C.-H., Park, J. & Cheong, H. Ising-Type Magnetic Ordering in Atomically Thin FePS3. (2016). at <http://arxiv.org/abs/1608.04169>

34. Wang, X., Du, K., Fredrik Liu, Y. Y., Hu, P., Zhang, J., Zhang, Q., Owen, M. H. S., Lu, X., Gan, C. K., Sengupta, P., Kloc, C. & Xiong, Q. Raman spectroscopy of atomically thin two-dimensional magnetic iron phosphorus trisulfide (FePS 3) crystals. *2D Mater.* **3,** 031009 (2016).

35. Gong, C., Li, L., Li, Z., Ji, H., Stern, A., Xia, Y., Cao, T., Bao, W., Wang, C., Wang, Y., Qiu, Z. Q., Cava, R. J., Louie, S. G., Xia, J. & Zhang, X. Discovery of intrinsic ferromagnetism in two-dimensional van der Waals crystals. *Nature* **546,** 265–269 (2017).

36. Gregory, N. W. Structural Properties of Chromium (II1) Iodide and Some Chromium (II1) Mixed Halides. **5049,** 1950–1952 (1958).

37. Hansen, W. N. & Griffel, M. Paramagnetic Susceptibilities of the Chromium (III) Halides. *J. Chem. Phys.* **30,** 913 (1959).

38. Seyler, K. L., Zhong, D., Klein, D. R., Gao, S., Zhang, X., Huang, B., Navarro-Moratalla, E., Yang, L., Cobden, D. H., McGuire, M. a., Yao, W., Xiao, D., Jarillo-Herrero, P. & Xu, X. Ligand-field helical luminescence in a 2D ferromagnetic insulator. *Nat. Phys.* 1–12 (2017). at

39. Anderson, P. W. Antiferromagnetism. Theory of superexchange interaction. *Phys. Rev.* **79,** 350–356 (1950).

40. Huang, B., Clark, G., Navarro-Moratalla, E., Klein, D. R., Cheng, R., Seyler, K. L., Zhong, D., Schmidgall, E., McGuire, M. a., Cobden, D. H., Yao, W., Xiao, D., Jarillo-Herrero, P. & Xu, X. Layer-dependent ferromagnetism in a van der Waals crystal down to the monolayer limit. *Nature* **546,** 270–273 (2017).

41. Sato, K. *Japanese Journal of Physics* **20.** (1981).

42. Haider, T. A Review of Magneto-Optic Effects and Its Application. *Int. J. Electromagn. Appl.* **7,** 17–24 (2017).

43. Weisheit, M., Weisheit, M., Fähler, S., Marty, A., Souche, Y., Poinsignon, C. & Givord, D. Electric Field – Induced Modification of Magnetism in Thin-Film Ferromagnets. *Science* **349,** (2011).

44. Chiba, D., Matsukura, F. & Ohno, H. Electric-field control of ferromagnetism in (Ga,Mn)As. *Appl. Phys. Lett.* **89,** 0–2 (2006).

45. Ohno, H., Chiba, D., Matsukura, F., Omiya, T., Abe, E., Dietl, T., Ohno, Y. & Ohtani, K. Electric-field control of ferromagnetism. *Nature* **408,** 944–946 (2000).

46. Ohno, H. Making Nonmagnetic Semiconductors Ferromagnetic. *Science (80).* **281,** 951–956 (1998).

47. Castellanos-Gomez, A., Buscema, M., Molenaar, R., Singh, V., Janssen, L., van der Zant, H. S. J. & Steele, G. a. Deterministic transfer of two-dimensional materials by all-dry viscoelastic stamping. *2D Mater.* **1,** 011002 (2014).

48. Huang, B., Clark, G., Klein, D. R., MacNeill, D., Navarro-Moratalla, E., Seyler, K. L., Wilson, N., McGuire, M. a., Cobden, D. H., Xiao, D., Yao, W., Jarillo-Herrero, P. & Xu, X. Electrical control of 2D magnetism in bilayer CrI3. *Nat. Nanotechnol.* **13,** 1–5 (2018).

49. Zhang, Y., Tang, T. T., Girit, C., Hao, Z., Martin, M. C., Zettl, A., Crommie, M. F., Shen, Y. R. & Wang, F. Direct observation of a widely tunable bandgap in bilayer graphene. *Nature* **459,** 820–823 (2009).

50. Taychatanapat, T., Watanabe, K., Taniguchi, T. & Jarillo-Herrero, P. Quantum Hall effect and Landau-level crossing of Dirac fermions in trilayer graphene. *Nat. Phys.* **7,** 621–625 (2011).

51. Klein, D. R., MacNeill, D., Lado, J. L., Soriano, D., Navarro-Moratalla, E., Watanabe, K., Taniguchi, T., Manni, S., Canfield, P., Fernández-Rossier, J. & Jarillo-Herrero, P. Probing magnetism in 2D van der Waals crystalline insulators via electron tunneling. *Science (80-.).* **1222,** 1–9 (2018).

52. Jiang, S., Li, L., Wang, Z., Mak, K. F. & Shan, J. Controlling magnetism in 2D CrI3by electrostatic doping. *Nat. Nanotechnol.* **13,** 549–553 (2018).

53. Frindt, R. F. The optical properties of single crystals of WSe$_2$ and MoTe$_2$. *J. Phys. Chem. Solids* **24,** 1107–1108 (1963).

54. Yang, D., Westreich, P. & Frindt, R. F. Transition metal dichalcogenide/polymer nanocomposites. *Nanostructured Mater.* **12,** 467–470 (1999).

55. Geim, a. K. & Novoselov, K. S. The rise of graphene. *Nat. Mater.* 183–191 (2007).

56. Chhowalla, M., Shin, H. S., Eda, G., Li, L.-J., Loh, K. P. & Zhang, H. The chemistry of two-dimensional layered transition metal dichalcogenide nanosheets. *Nat. Chem.* **5,** 263–275 (2013).

57. Wang, Q. H., Kalantar-Zadeh, K., Kis, A., Coleman, J. N. & Strano, M. S. Electronics and optoelectronics of two-dimensional transition metal dichalcogenides. *Nat. Nanotechnol.* **7,** 699–712 (2012).

58. Schaibley, J. R., Yu, H., Clark, G., Rivera, P., Ross, J. S., Seyler, K. L., Yao, W. & Xu, X. Valleytronics in 2D materials. *Nat. Rev. Mater.* **1,** 16055 (2016).

59. Liu, G.-B., Shan, W.-Y., Yao, Y., Yao, W. & Xiao, D. Three-band tight-binding model for monolayers of group-VIB transition metal dichalcogenides. *Phys. Rev. B* **88,** 085433 (2013).

60. Xiao, D., Liu, G.-B., Feng, W., Xu, X. & Yao, W. Coupled Spin and Valley Physics in Monolayers of MoS_2 and Other Group-VI Dichalcogenides. *Phys. Rev. Lett.* **108,** 196802 (2012).

61. Mak, K. F., He, K., Shan, J. & Heinz, T. F. Control of valley polarization in monolayer MoS2 by optical helicity. *Nat. Nanotechnol.* **7,** 494–498 (2012).

62. Wu, S., Ross, J. S., Liu, G.-B., Aivazian, G., Jones, A., Fei, Z., Zhu, W., Xiao, D., Yao, W., Cobden, D. & Xu, X. Electrical tuning of valley magnetic moment through symmetry control in bilayer MoS2. *Nat. Phys.* **9,** 149–153 (2013).

63. Xu, X., Yao, W., Xiao, D. & Heinz, T. F. Spin and pseudospins in layered transition metal dichalcogenides. *Nat. Phys.* **10,** 343–350 (2014).

64. Gunawan, O., Shkolnikov, Y. P., Vakili, K., Gokmen, T., De Poortere, E. P. & Shayegan, M. Valley Susceptibility of an Interacting Two-Dimensional Electron System. *Phys. Rev. Lett.* **97,** 186404 (2006).

65. Landin, L. Optical Studies of Individual InAs Quantum Dots in GaAs: Few-Particle Effects. *Science (80).* **280,** 262–264 (1998).

66. Grundmann, M., Christen, J., Ledentsov, N. N., Böhrer, J., Bimberg, D., Ruvimov, S. S., Werner, P., Richter, U., Gösele, U., Heydenreich, J., Ustinov, V. M., Egorov, a. Y.,

Zhukov, a. E., Kop'ev, P. S. & Alferov, Z. I. Ultranarrow Luminescence Lines from Single Quantum Dots. *Phys. Rev. Lett.* **74,** 4043–4046 (1995).

67. Reithmaier, J. P., Sek, G., Löffler, a, Hofmann, C., Kuhn, S., Reitzenstein, S., Keldysh, L. V, Kulakovskii, V. D., Reinecke, T. L. & Forchel, a. Strong coupling in a single quantum dot-semiconductor microcavity system. *Nature* **432,** 197–200 (2004).

68. Warburton, R., Schaflein, C., Haft, D., Bickel, F., Lorke, a, Karrai, K., Garcia, J., Schoenfeld, W. & Petroff, P. Optical emission from a charge-tunable quantum ring. *Nature* **405,** 926–9 (2000).

69. Kurtsiefer, C., Mayer, S., Zarda, P. & Weinfurter, H. Stable solid-state source of single photons. *Phys. Rev. Lett.* **85,** 290–293 (2000).

70. Koehl, W. F., Buckley, B. B., Heremans, F. J., Calusine, G. & Awschalom, D. D. Room temperature coherent control of defect spin qubits in silicon carbide. *Nature* **479,** 84–87 (2011).

71. Eda, G., Yamaguchi, H., Voiry, D., Fujita, T., Chen, M. & Chhowalla, M. Photoluminescence from chemically exfoliated MoS 2. *Nano Lett.* **11,** 5111–5116 (2011).

72. Ugeda, M. M., Bradley, A. J., Shi, S.-F., da Jornada, F. H., Zhang, Y., Qiu, D. Y., Ruan, W., Mo, S.-K., Hussain, Z., Shen, Z.-X., Wang, F., Louie, S. G. & Crommie, M. F. Giant bandgap renormalization and excitonic effects in a monolayer transition metal dichalcogenide semiconductor. *Nat. Mater.* **13,** 1091–1095 (2014).

73. Van der Zande, A. M., Huang, P. Y., Chenet, D. a, Berkelbach, T. C., You, Y., Lee, G.-H., Heinz, T. F., Reichman, D. R., Muller, D. a & Hone, J. C. Grains and grain boundaries in highly crystalline monolayer molybdenum disulphide. *Nat. Mater.* **12,** 554–61 (2013).

74. Polarization, N. V., Wu, S., Huang, C., Aivazian, G., Ross, J. S. & Cobden, D. H. Vapor À Solid Growth of High Optical Quality MoS 2 Monolayers with. 2768–2772 (2013). doi:10.1021/nn4002038

75. Huang, J. K., Pu, J., Hsu, C. L., Chiu, M. H., Juang, Z. Y., Chang, Y. H., Chang, W. H., Iwasa, Y., Takenobu, T. & Li, L. J. Large-area synthesis of highly crystalline WSe2 monolayers and device applications. *ACS Nano* **8,** 923–930 (2014).

76. Huang, C., Wu, S., Sanchez, A. M., Peters, J. J. P., Beanland, R., Ross, J. S., Rivera, P., Yao, W., Cobden, D. H. & Xu, X. Lateral heterojunctions within monolayer MoSe2–WSe2 semiconductors. *Nat. Mater.* **13,** 1096–1101 (2014).

77. Lv, R., Robinson, J. a., Schaak, R. E., Sun, D., Sun, Y., Mallouk, T. E. & Terrones, M. Transition metal dichalcogenides and beyond: Synthesis, properties, and applications of single- and few-layer nanosheets. *Acc. Chem. Res.* **48,** 56–64 (2015).

78. Jones, A. M., Yu, H., Ghimire, N. J., Wu, S., Aivazian, G., Ross, J. S., Zhao, B., Yan, J., Mandrus, D. G., Xiao, D., Yao, W. & Xu, X. Optical generation of excitonic valley coherence in monolayer WSe2. *Nat. Nanotechnol.* **8,** 634–638 (2013).

79. Ross, J. S., Wu, S., Yu, H., Ghimire, N. J., Jones, A. M., Aivazian, G., Yan, J., Mandrus, D. G., Xiao, D., Yao, W. & Xu, X. Electrical control of neutral and charged excitons in a monolayer semiconductor. *Nat. Commun.* **4,** 1474 (2013).

80. He, Y.-M., Clark, G., Schaibley, J. R., He, Y., Chen, M.-C., Wei, Y.-J., Ding, X., Zhang, Q., Yao, W., Xu, X., Lu, C.-Y. & Pan, J.-W. Single quantum emitters in monolayer semiconductors. *Nat. Nanotechnol.* (2015). doi:10.1038/nnano.2015.75

81. Tonndorf, P., Schmidt, R., Schneider, R., Kern, J., Buscema, M., Steele, G., Castellanos-Gomez, A., Zant, H. S. J. Van Der, Vasconcellos, S. M. De & Bratschitsch, R. Single-photon emission from localized excitons in an atomically thin semiconductor. *Optica* **2,** 347–352 (2015).

82. Chakraborty, C., Kinnischtzke, L., Goodfellow, K. M., Beams, R. & Vamivakas, a. N. Voltage-controlled quantum light from an atomically thin semiconductor. *Nat. Nanotechnol.* **10,** 507–511 (2015).

83. Srivastava, A., Sidler, M., Allain, A. V., Lembke, D. S., Kis, A. & Imamoğlu, a. Optically active quantum dots in monolayer WSe2. *Nat. Nanotechnol.* **10,** 491–496 (2015).

84. Koperski, M., Nogajewski, K., Arora, a., Cherkez, V., Mallet, P., Veuillen, J.-Y., Marcus, J., Kossacki, P. & Potemski, M. Single photon emitters in exfoliated WSe2 structures. *Nat. Nanotechnol.* **10,** 503–506 (2015).

85. Aivazian, G., Gong, Z., Jones, a M., Chu, R. L., Yan, J., Mandrus, D. G., Zhang, C., Cobden, D., Yao, W. & Xu, X. D. Magnetic Control of Valley Pseudospin in Monolayer WSe2. *arXiv* **1406,** 2546 (2014).

86. Srivastava, A., Sidler, M., Allain, A. V, Lembke, D. S., Kis, A. & Imamoglu, a. Valley Zeeman effect in elementary optical excitations of monolayer WSe2. *Nat. Phys.* **11,** 141–147 (2015).

87. Bayer, M., Ortner, G., Stern, O., Kuther, a., Gorbunov, a. a., Forchel, a., Hawrylak, P., Fafard, S., Hinzer, K., Reinecke, T. L., Walck, S. N., Reithmaier, J. P., Klopf, F. & Schäfer, F. Fine structure of neutral and charged excitons in self-assembled In(Ga)As/(Al)GaAs quantum dots. *Phys. Rev. B* **65,** 195315 (2002).

88. Yu, H., Liu, G. Bin, Gong, P., Xu, X. & Yao, W. Dirac cones and Dirac saddle points of bright excitons in monolayer transition metal dichalcogenides. *Nat. Commun.* **5,** 1–7 (2014).

89. Withers, F., Del Pozo-Zamudio, O., Schwarz, S., Dufferwiel, S., Walker, P. M., Godde, T., Rooney, a. P., Gholinia, a., Woods, C. R., Blake, P., Haigh, S. J., Watanabe, K., Taniguchi, T., Aleiner, I. L., Geim, a. K., Fal'Ko, V. I., Tartakovskii, a. I. & Novoselov, K. S. WSe2 Light-Emitting Tunneling Transistors with Enhanced Brightness at Room Temperature. *Nano Lett.* **15,** 8223–8228 (2015).

90. Palacios-Berraquero, C., Kara, D. M., Montblanch, A. R. P., Barbone, M., Latawiec, P., Yoon, D., Ott, A. K., Loncar, M., Ferrari, A. C. & Atatüre, M. Large-scale quantum-emitter arrays in atomically thin semiconductors. *Nat. Commun.* **8,** 1–6 (2017).

91. Geim, a K. & Grigorieva, I. V. Van der Waals heterostructures. *Nature* **499,** 419–25 (2013).

92. Ohno, H., Munekata, H., Penney, T., Vonmolnar, S. & Chang, L. L. Magnetotransport Properties of p-Type (In,Mn) As Diluted Magnetic III-V Semiconductors. *Phys. Rev. Lett.* **68,** 2664–2667 (1992).

93. Lee, B., Jungwirth, T. & MacDonald, a. Theory of ferromagnetism in diluted magnetic semiconductor quantum wells. *Phys. Rev. B* **61,** 15606–15609 (2000).

94. Munekata, H., Ohno, H., Von Molnar, S., Segm̈ller, A., Chang, L. L. & Esaki, L. Diluted magnetic III-V semiconductors. *Phys. Rev. Lett.* **63,** 1849–1852 (1989).

95. Crooker, S. a., Tulchinsky, D. a., Levy, J., Awschalom, D. D., Garcia, R. & Samarth, N. Enhanced spin interactions in digital magnetic heterostructures. *Phys. Rev. Lett.* **75,** 505–508 (1995).

96. Crooker, S. a., Awschalom, D. D., Baumberg, J. J., Flack, F. & Samarth, N. Optical spin resonance and transverse spin relaxation in magnetic semiconductor quantum wells. *Phys. Rev. B* **56,** 7574–7588 (1997).

97. Zeng, H., Dai, J., Yao, W., Xiao, D. & Cui, X. Valley polarization in MoS2 monolayers by optical pumping. *Nat. Nanotechnol.* **7,** 490–493 (2012).

98. Rostami, H. & Asgari, R. Valley Zeeman effect and spin-valley polarized conductance in monolayer MoS2 in a perpendicular magnetic field. *Phys. Rev. B - Condens. Matter Mater. Phys.* **91,** 1–11 (2015).

99. Stier, A. V., McCreary, K. M., Jonker, B. T., Kono, J. & Crooker, S. a. Exciton diamagnetic shifts and valley Zeeman effects in monolayer WS2 and MoS2 to 65 Tesla. *Nat. Commun.* **7,** 10643 (2016).

100. Haugen, H., Huertas-Hernando, D. & Brataas, A. Spin transport in proximity-induced ferromagnetic graphene. *Phys. Rev. B - Condens. Matter Mater. Phys.* **77,** 1–8 (2008).

101. Wang, Z., Tang, C., Sachs, R., Barlas, Y. & Shi, J. Proximity-induced ferromagnetism in graphene revealed by the anomalous hall effect. *Phys. Rev. Lett.* **114,** 1–5 (2015).

102. Wei, P., Lee, S., Lemaitre, F., Pinel, L., Cutaia, D., Cha, W., Katmis, F., Zhu, Y., Heiman, D., Hone, J., Moodera, J. S. & Chen, C.-T. Strong interfacial exchange field in the graphene/EuS heterostructure. *Nat. Mater.* **15,** 711–716 (2016).

103. Yang, H. X., Hallal, a., Terrade, D., Waintal, X., Roche, S. & Chshiev, M. Proximity effects induced in graphene by magnetic insulators: First-principles calculations on spin filtering and exchange-splitting gaps. *Phys. Rev. Lett.* **110,** 1–5 (2013).

104. Zhong, D., Seyler, K. L., Linpeng, X., Cheng, R., Sivadas, N., Huang, B., Schmidgall, E., Taniguchi, T., Watanabe, K., McGuire, M. a., Yao, W., Xiao, D., Fu, K.-M. C. & Xu, X. Van der Waals engineering of ferromagnetic semiconductor heterostructures for spin and valleytronics. *Sci. Adv.* **3,** e1603113 (2017).

105. Yuan, H., Liu, X., Afshinmanesh, F., Li, W., Xu, G., Sun, J., Lian, B., Curto, A. G., Ye, G., Hikita, Y., Shen, Z., Zhang, S.-C., Chen, X., Brongersma, M., Hwang, H. Y. & Cui, Y. Polarization-sensitive broadband photodetector using a black phosphorus vertical p–n junction. *Nat. Nanotechnol.* **10,** 707–713 (2015).

VITA

Genevieve Clark was born in Mountain View, CA to David and Lesley Clark and was raised in Windham, NH. After high school she attended McGill University, where she had the opportunity to conduct research on optical properties of gold and silver nanoparticles and ultrafast spectroscopy of colloidal quantum dots, and develop an interest in optical spectroscopy. After graduating with a Bsc in Chemistry she began graduate school at University of Washington in Materials Science & Engineering in September 2013.

Publications:

‘Optical Control of magnetic behavior in WSe_2-CrI_3 heterostructures’
Clark, G., *et al.* (In preparation)

‘Ultra-Long Lifetimes of Single Quantum Emitters in Monolayer WSe_2-hBN Heterostructures’
Chandriker, D., Khan, M., **Clark, G.**, Simon, J., Gibson, R., Mou, S., Xu, X., Leuenberger, M., Hendrickson, J. *Nat. Commun.* (Submitted)

‘Electrical Control of 2D Magnetism in Bilayer CrI_3’
Huang, B.*, **Clark, G.*,** Klein, D*. *et al. Nat. Nanotechnol*. (2018)

‘Radiative control of dark excitons at room temperature by nano-optical antenna-tip Purcell effect’
Park, K-D., Jiang, T., **Clark, G.**, Xu, X., Raschke, M. *Nat. Nanotechnol.* **13** 59-64 (2018)

‘Layer Dependent Ferromagnetism in a van der Waals Crystal down to the Monolayer Limit’
Huang, B.*, **Clark, G.***, Navarro-Moratalla, E.*, *et al.* *Nature* **546** 270-273 (2017)

‘Magnetic Behavior and Spin-Lattice Coupling in Cleavable van der Waals Layered CrCl3 Crystals’
McGuire, M., **Clark, G.**, Santosh, K., Chance, M., Ellison, J., Cooper, V., Xu, X., Sales, B. *Phys. Rev. Materials* **1** 014001 (2017)

‘Nanocavity-Integrated van der Waals Heterostructure Light-Emitting Tunneling Diode’
Liu, C-H., **Clark, G.**, Fryett, T., Wu, S., Zheng, J., Hatami, F., Xu, X., Majumdar, A. *Nano Lett.* **17(1)** 200-205 (2017)

‘Dynamic optical tuning of interlayer interactions in the monolayer transition metal dichalcogenides’
Mannebach, E., *et al. Nano Lett.* **17(12)** 7761-7766 (2017)

‘Single defect light-emitting diode in a van der Waals heterostructure’
Clark, G. *et al.* *Nano Lett.* **16(6)** 3944-3948 (2016)

‘Valleytronics in 2D Materials’
Schaibley, J., Yu, H., **Clark, G.**, Rivera, P., Ross, J., Seyler, K., Yao, W., Xu, X. *Nat. Rev. Mater.* **1** 16055 (2016)

‘Probing the influence of dielectric environment on excitons in monolayer WSe_2: insight from high magnetic fields’
Stier, A., Wilson, N., **Clark, G.**, Xu, X, Crooker, S. *Nano. Lett.* **16(11)**, 7054-7060, (2016)

‘Hybrid tip-enhanced nano-spectroscopy and –imaging of monolayer WSe_2 with local strain control’

Park, K-D., Khatib, O., Kravtsov, V., **Clark, G.**, Xu, X., Raschke, M. *Nano Lett.* **16(4)**, 2621-2627 (2016)

'Single Quantum Emitters in Monolayer Semiconductors'
He, Y-M., **Clark, G.**, Schaibley, J., He, Y., Chen, M-C., Wei, Y-J., Ding, X., Zhang, Q., Yao, W., Xu, X., Lu, C-Y., Pan, J-W. *Nat. Nanotechnol.* **10** 497-502 (2015)

'Observation of long-lived interlayer excitons in monolayer $MoSe_2$-WSe_2 heterostructures'
Rivera, P., Schaibley, J., Jones, A., Ross, J., Wu, S., Aivazian, G., Klement, P., Seyler, K., **Clark, G.**, Ghimire, N., Yan, J., Mandrus, D., Yao, W., Xu, X. *Nat. Commun.* **6** 6242 (2015)

'Intrinsic homogeneous linewidth and broadening mechanisms of excitons in monolayer transition metal dichalcogenides'
Moody, G. *et al.* Nat. Commun. **6** 8315 (2015)

'Vapor-transport growth of high optical quality WSe_2 monolayers'
Clark, G. *et al. APL Materials*, **2**, 101101 (2014)